Physics of Fluids

Experiment on jet-vortex interaction for variable mutual spacing

Accepted Manuscript: This article has been accepted for publication and undergone full peer review but has not been through the copyediting, typesetting, pagination, and proofreading process, which may lead to differences between this version and the Version of Record.

Cite as: Physics of Fluids (in press) (2022); https://doi.org/10.1063/5.0127634
Submitted: 23 September 2022 • Accepted: 09 December 2022 • Accepted Manuscript Online: 11 December 2022

Tobias Bölle, Vincent Brion, Marie Couliou, et al.

View Online
Export Citation
CrossMark

ARTICLES YOU MAY BE INTERESTED IN

Unsteady Flow past slotted circular cylinders in laminar regime: Effect of slit shapes and Reynolds number
Physics of Fluids (2022); https://doi.org/10.1063/5.0130736

Physics of Fluids

Special Topic: Food Physics

Submit Today!

AIP Publishing

Physics of Fluids (in press) (2022); https://doi.org/10.1063/5.0127634

(c) 2022 Author(s).

Accepted to Phys. Fluids 10.1063/5.0127634

Experiment on jet–vortex interaction for variable mutual spacing

Tobias Bölle,[1] Vincent Brion,[2] Marie Couliou,[2] and Pascal Molton[2]

[1] *Deutsches Zentrum für Luft- und Raumfahrt, Institut für Physik der Atmosphäre, Oberpfaffenhofen, Germany*

[2] *DAAA, ONERA, Université Paris-Saclay, 92120, France*

(*tobias.boelle@dlr.de)

(Dated: 2 December 2022)

The interaction of a line vortex with a collinearly aligned jet is a prototypical configuration for various important applications in aeronautics. The purpose of this study is to analyze the impact of the jet flow on the kinematics and dynamics of a trailing vortex. A particular emphasis is on the effect of a variable relative jet–vortex spacing. To this end, we realized four different jet–vortex configurations in a wind-tunnel experiment at chord-based Reynolds number of 1.7×10^5 using high-speed stereo particle image velocimetry measurements in five transversal planes located between 2 and 26 chords behind the wing. Stochastic analyses reveal that the jet generally contributes an external excitation to the vortex as a function of the mutual spacing. Compared with the configuration without jets, the vortex amplification increases upon reducing the jet–vortex spacing. Most notably, for all but the closest spacing, the vortex response is qualitatively the same, changing mainly in magnitude. For the closest spacing, however, the dynamics is considerably different, which we suspect to be a consequence of jet entrainment. Proper orthogonal decomposition reveals, for the first time, that the collinearly aligned jet tends to excite a progressively broader range of vortex modes as the jet–vortex spacing is reduced. Close examination of the vortex mean flow seems to preclude linear vortex instabilities, while the vortex characteristics hint towards some form of receptivity mechanism to disturbances being located in the free stream. Our analyses are useful to validate simulation tools on configurations combining simultaneous lift and thrust effects.

I. INTRODUCTION

The kinematics and dynamics of jet–vortex interaction constitute fundamental problems in fluid dynamics. In particular, it is the prototypical configuration of the near airplane wake and, as such, has important bearings on the wake evolution and its impact on the environment[1,2]. Hence, an understanding of the kinematic and dynamic characteristics is of central interest both for control strategies to efficiently reduce the hazard of wake encounters[3] and for the initial formation stages of contrails[4,5]. The long persistence of trailing vortices of the order of $10\,\mathrm{km}$ ($\sim 10^3 c$ assuming a chord length $c \sim 10\,\mathrm{m}$)[6] or equivalently 10^2 s (assuming a flight speed of the order of $10^2\ \mathrm{m\,s^{-1}}$)[2] makes them the principal hazard for following aircraft[3,7]. Efficient control strategies are thus in need that accelerate their alleviation. Our focus in this study will be on the effect of the jet on the trailing vortex with a particular emphasis on a variable relative jet–vortex spacing. The importance of the relative spacing for the efficiency of control applications has also been noted by[4,8]. Our configuration has some conceptual similarity with studies on the (synthetic-)jet actuation of vortices in a control context[9–13].

Simulations of jet–vortex interaction mostly relied on idealized initial and boundary conditions, i.e., computations are carried out in a (streamwise) periodic domain, initialized with the superposition of a line vortex (Lamb–Oseen, vortex filament) and a (Gaussian) jet flow[1,5,14–18]. Since, the near and intermediate wake generally deserved much less attention than the far wake, these initial-boundary conditions are an acceptable approximation[14,16]. However, the first phase of the wake evolution, called *jet regime*, is spatially developing and poorly represented by such simplified initial-boundary conditions. The jet regime refers to the wake dynamics in approximately the first $10\,\mathrm{s}$[1,2]. Taking the order-of-magnitude estimates $10^2\ \mathrm{m\,s^{-1}}$ and $10\,\mathrm{m}$ for airplane cruise speed and chord length, respectively, leads to a downstream range of about $10^2 c$. The consequences of spatially rather than temporally developing dynamics on the jet regime are highlighted as a future issue by[2].

Due to the the associated numerical difficulties, the near wake has been analyzed mainly experimentally. Most of these experiments focused on detailed analyses of the very-near wake up to one[4,9], four[19] and eight chords[12] behind the wing. A larger downstream range in the same jet–vortex configuration as studied here, has been analyzed by[15,20] using laser doppler velocimetry. These two studies emphasized the effect of the vortex on the distribution and entrainment of the jet exhaust. Regarding the reverse interaction,[20] found that the jets have a small influence on the mean vortex characteristics (mean velocity fields and mean centre location). However, the vortex fluctuation dynamics was observed to be enhanced by the presence of the jets. The objective of the present study is a detailed characterization and discussion of the mean and fluctuation fields of the vortex up to 26 chords behind the wing with a particular emphasis on the effect of variable jet positioning. To this end, we conducted high-speed stereo particle image velocimetry (PIV) measurements for the same configuration as[15,20].

The paper is structured as follows. In § II, we present the experimental setting, instrumentation and the different jet–vortex configurations analyzed. The subsequent analyses of the experimental data describe the kinematics and dynamics of the trailing vortex on the basis of the leading-stochastic moments. After discussing the mean vortex flow in § III, the characterization of the unsteady vortex kinematics and dynamics is detailed in § IV. Our analysis of the vortex-centre motion in § IV A is complemented by a discussion of the unsteady vortex dynamics in terms of Reynolds stresses in § IV B and a proper orthogonal decomposition in§ IV C. We terminate with a conclusion of the main results in § V.

II. EXPERIMENTAL CONFIGURATION AND MEASUREMENT TECHNIQUE

A. Apparatus

Experiments were conducted at the ONERA centre in Le Fauga-Mauzac in an atmospheric, closed-circuit wind tunnel having a rectangular test section of 1.4 m width, 1.8 m height at the entrance evolving to 1.85 m at the exit and 5.0 m length. The divergence of the upper and lower walls (ceiling-floor) at an angle of 0.58° compensates for the streamwise velocity gradient induced by the development of the boundary layer along the test section walls. The turbulence intensity in the empty wind tunnel is less than 0.5 %.

The test configuration probed in this study consists of a rectangular wing with two jet generators placed underneath and is identical to the setting studied in[20]. Schematics of the different views of the set up are shown in Fig. 1 along with photographs of the installation and the relevant details in Fig. 2.

The vortex is generated by an airfoil with NACA0012 symmetric profile of chord length $c = 0.125\,\mathrm{m}$ and wing span $b = 0.5\,\mathrm{m}$, which is suspended from the wind-tunnel ceiling by a NACA0015 profile with a chord length of 0.045 m. Stabilizing cables have been tensed to prevent

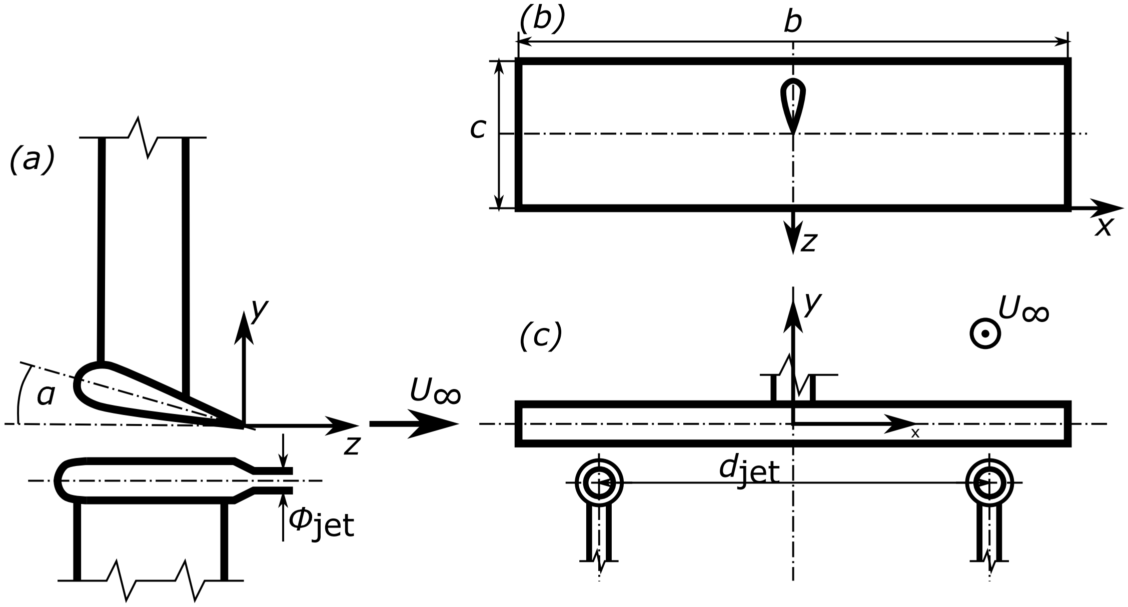

FIG. 1. Schematic of the experimental installation. (*a*) side view, (*b*) top view, (*c*) view from the back.

lateral oscillations as can be seen in Fig. 2*a*. The wing is placed in the center of the test section, with the leading edge set at a distance 0.695 m (or $5.56c$) downstream of the inlet section, corresponding to the end of the nozzle of the wind tunnel. The wing tips are located 0.454 m (or $3.63c$) from the test section side walls. Boundary-layer transition over the airfoil is triggered by a saw-tooth shaped tape of 6 mm width and 0.205 mm thickness placed $z = 6.5\,\mathrm{mm}$ (5.2 % of the chord length) downstream of the leading edge. The wing is set at a constant angle of incidence of $\alpha = 9^\circ$.

Two identical jet generators are mounted on NACA0015 supporting structures with 0.1 m chord length from the wind-tunnel floor. Their axes are positioned at a height 0.876 m above the floor, which yields a distance of 0.142 m below the wing trailing edge. The lateral jet position is variable and three different locations associated with a mutual spacing of $d_{\mathrm{jet}}/b \in \{0.44, 0.58, 0.80\}$ have been assessed (cf. Figs. 1*a*,*c* and Fig. 2*b*). Boundary-layers transition is triggered along the external side of the jet casing and the supporting structures by means of bands of 0.3 mm carborundum grains set at an axial distance of 0.011 m from the leading edges of the jet casing. The jet-generator exit has a diameter of $\phi_{\mathrm{jet}} = 0.01\,\mathrm{m}$ and is equipped with an internal perforated plate of 1.5 mm hole diameter in order to homogenize the jet flow (see Fig. 2). Note that, unlike[20], the jets are not heated. The velocity of the jet is designated as the velocity corresponding to the mass flow rate and is set to $U_{\mathrm{jet}} = 50.2\,\mathrm{m\,s^{-1}}$. It serves as a rough estimate of the flow velocity in the jet core.

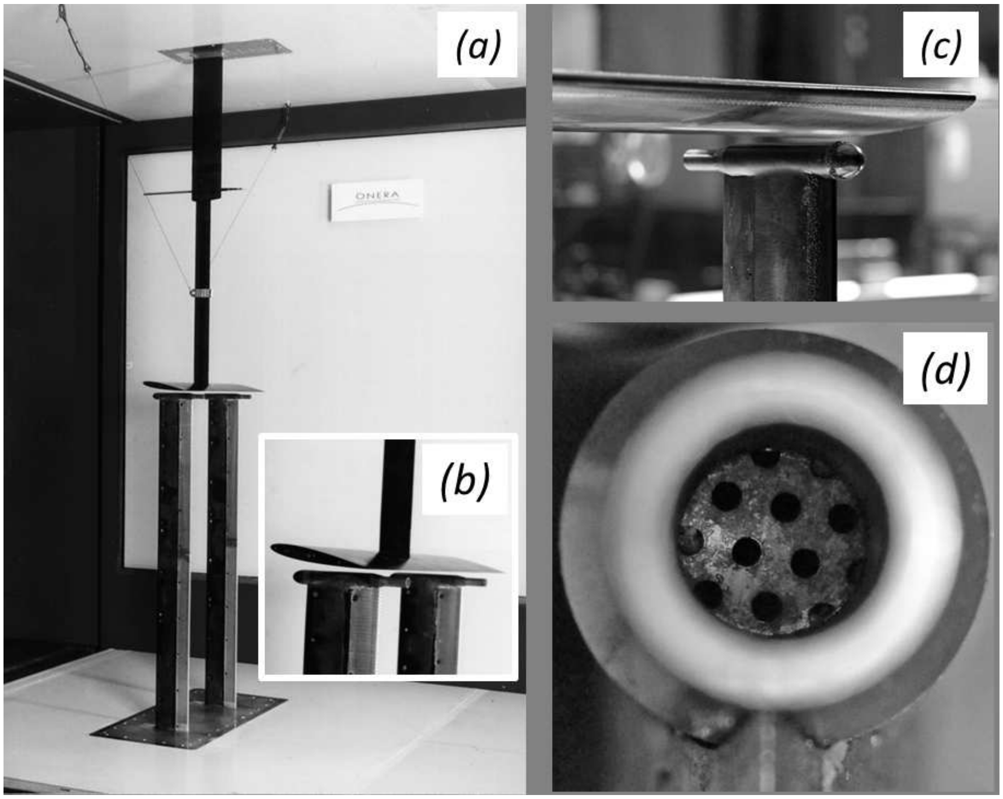

FIG. 2. Photographs showing the experimental installation. (a) global installation showing the suspended wing with the bottom-mounted jets, (b) detail of the wing and the jets, (c) details of the transition devices, (d) detail of the jet outlet geometry and internal grid.

The jet momentum and wing angle of incidence are realistic for a typical lift and drag balance of an aircraft in cruise condition.

For all experiments, the free-stream velocity was set at $U_\infty = 20\,\mathrm{m\,s^{-1}}$ implying a chord-based Reynolds number of $R_c := cU_\infty/\nu \approx 1.7 \times 10^5$. As shown in Fig. 1, the Cartesian coordinate system is attached to the trailing edge in the symmetry plane with the coordinates x, y, z being positive starboard, vertically upwards and in the direction of the mean free-stream velocity U_∞, respectively. For convenience, the spatial coordinates are split into the cross-stream coordinate tuple $\boldsymbol{x} = (x, y) \in M \subset R^2$ in the measurement plane M at fixed streamwise coordinate z.

B. Instrumentation and configurations

Stereo Particle Image Velocimetry (PIV) was used in five transversal planes downstream of the test model to measure the two-dimensional, 3-component velocity field $\boldsymbol{u}(t, \boldsymbol{x}) = (u(t, \boldsymbol{x}), v(t, \boldsymbol{x}), w(t, \boldsymbol{x}))$.

The measurement planes are located at the constant streamwise coordinates $z \in \{250, 500, 1545, 2500, 3280\}$ mm, corresponding approximately to dimensionless $z/c \in \{2, 4, 12, 20, 26\}$.

The wind tunnel was seeded with DEHS (di-2-ethylhexyl sebacate) tracer particles of density $0.91\,\mathrm{g\,cm^{-3}}$ and mean particle size of the order of $0.5\,\mu\mathrm{m}$ (always less than $1\,\mu\mathrm{m}$). The laser sheet is generated by an ND:YLF pulsed Litron laser system with green visible light of 527 nm wavelength and 25 mJ per pulse. The PIV images are captured by two V710 PHANTOM cameras (maximal image rate of 7.5 kHz) equipped with a NIKON objective with 105 mm focus and Scheimpflug adapter. The cameras are placed opposite to the laser with respect to the sides walls and at each side of the measurement planes. Forward scattering mode is hence achieved. The calibration of the PIV images is realized using a LAVISION $0.3\,\mathrm{m} \times 0.3\,\mathrm{m}$ calibration body. The image acquisition is realized with the DAVIS 8.2.2 program of LAVISION at a resolution of 1280 pixels × 800 pixels with a pixel size of $20\,\mu\mathrm{m} \times 20\,\mu\mathrm{m}$. In each configuration and measurement plane, 10 blocks of $N = 4096$ images are taken at a sampling frequency of $f_s = 3\,\mathrm{kHz}$, corresponding to a measurement time $T = N/f_s \approx 1.37\,\mathrm{s}$.

The reconstruction of the velocity field $\boldsymbol{u} = (u, v, w) = (u_i)$ ($i = 1, \ldots, 3$ along the coordinates (x, y, z), respectively) uses the Lucas–Kanade method to solve the optical-flow problem in a multi-resolution Gaussian pyramid approach in order to prevent convergence to local extrema. This is implemented in the FOLKI software of ONERA, which is also used to compute the streamwise vorticity $\omega = \partial u/\partial y - \partial v/\partial x$[21]. Windows of 31 pixels × 31 pixels are used, which yields a spatial resolution of the PIV data of approximately 7 mm.

Four different configurations are analyzed. We call *no-jet* configuration the reference case of the wing alone without the jet generators. Furthermore, three different *jet–vortex* configurations with relative spacing $d_{\mathrm{jet}}/b \in \{0.44, 0.58, 0.80\}$ as shown in Fig. 1 have been assessed. The position $d_{\mathrm{jet}}/b = 0.80$ corresponds roughly to the position of the rolled-up tip vortex and thus deserves a special attention, as we confirm later on.

C. Characterization of the jet flow

In order to characterize the unperturbed jet flow, PIV measurements have been conducted without the wing model and seeding the jets only. Additionally, the streamwise veolocity w of the jet flow was measured using hot wires (DANTEC 55P11) placed 1 mm downstream of the jet-exit plane. To measure the whole jet flow, a totality of 169 hot-wire measurements were taken, whereas

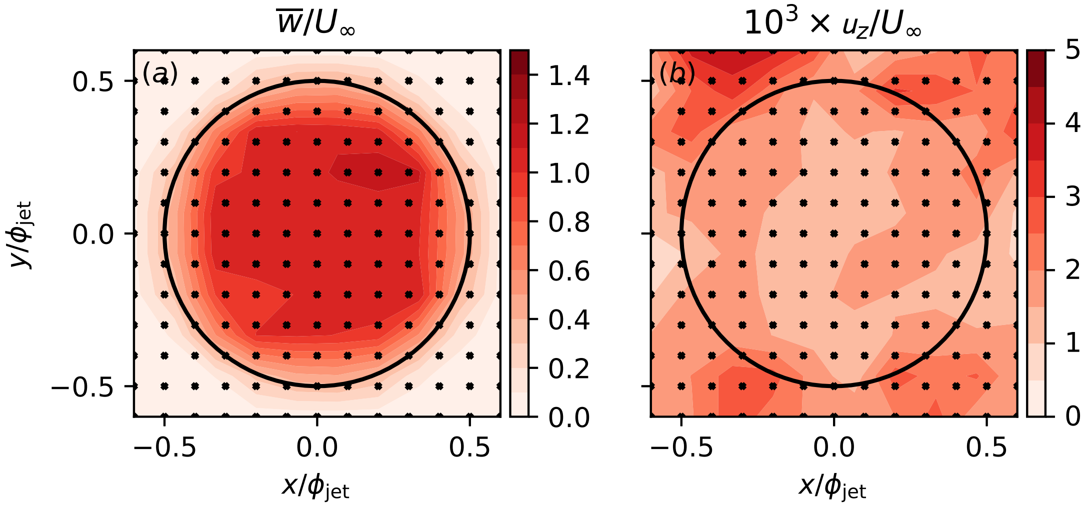

FIG. 3. Hot-wire measurements of the mean and turbulence characteristics of the jet flow at the exit nozzle. (a) streamwise component of the mean velocity $\bar{w}/U_{\text{jet}}$, (b) streamwise component of the turbulence intensity $10^3 \times u_z/U_{\text{jet}}$. The markers indicate the measurement matrix and the solid circle the jet nozzle exit outer edge.

a single hot wire was placed at either one of the nodes of a 13×13 test matrix. The 196 hot-wire probing locations, equi-spaced at 0.5 mm (i.e., $0.05\phi_{\text{jet}}$), are shown in Fig. 3.

Figures 3–5 show the mean and turbulence characteristics of the jet flow at the jet nozzle using hot-wire measurements (Fig. 3–4) and at $z/c = 1$ using PIV measurements (Fig. 5). The streamwise component of the mean velocity is normalized on U_{jet} (the mean being defined in (2)) and the turbulence intensity is defined as

$$u := \sqrt{\frac{1}{3}\sum_{i=1}^{3}\overline{u_i'^2}}. \tag{1}$$

where a prime indicates a fluctuation due to Reynolds decomposition (see § III). In the case of the hot-wire measurements only the streamwise component $u_z := \sqrt{\overline{u_3'^2}}$ of (1) is available.

The hot-wire measurements at the jet-exit nozzle (Fig. 3–4) show that the streamwise mean velocity $\bar{w}$ is close to U_{jet}, although the jet is not perfectly axisymmetric yet. In particular, the mean-flow profiles shown in Fig. 4 display a left-right asymmetry. The streamwise turbulence intensity of the jet flow at the exit nozzle of $u_z/U_{\text{jet}} \lesssim 5 \times 10^{-3}$ is of the same order of magnitude as the free-stream turbulence in the empty wind tunnel.

In order to illustrate the downstream evolution of the jet, Fig. 5 additionally shows the stream-

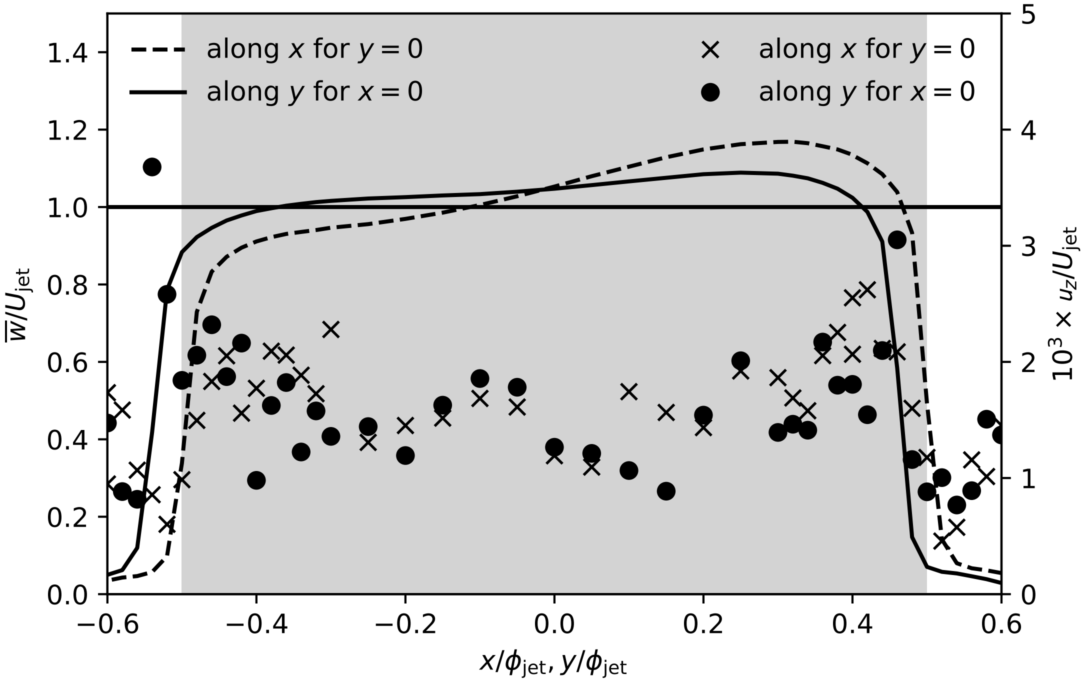

FIG. 4. Hot-wire measurements across the jet at the exit nozzle. Solid (dashed) line shows the streamwise component of the mean velocity along a vertical (horizontal) line across the jet centre. Dots (crosses) show the streamwise component of the turbulence intensity along a vertical (horizontal) line across the jet centre. The extent of the jet nozzle exit plane is indicated by grey shading.

wise mean velocity and full turbulence intensity (1) at $z/ = 1$ (or equivalently $z/\phi_{\mathrm{jet}} = 12.5$) obtained with PIV. We observe that both fields are essentially axisymmetric. The contribution from the transversal components of the mean velocity $\bar{u}$ and $\bar{v}$ are about one to two orders of magnitude less than $\bar{w}$ (not shown). The jet flow spreads laterally while preserving a nearly axisymmetric structure up to $z/c \approx 7$ downstream of the exit nozzle (not shown). The radius of the jet evolves from $0.055\phi_{\mathrm{jet}}$ to $2\phi_{\mathrm{jet}}$ over the chord-length separation between the hot-wire and PIV measurement planes in Fig. 4(a) and Fig. 5(a), respectively. The resulting spreading rate of the round jet is about 0.12, in close agreement with the regular value of 0.1[22]. The turbulence intensity increases sharply within the same distance, from 0.5 % to 12 %, with respect to the jet velocity U_{jet}, as a consequence of the turbulent activity in the jet shear layer.

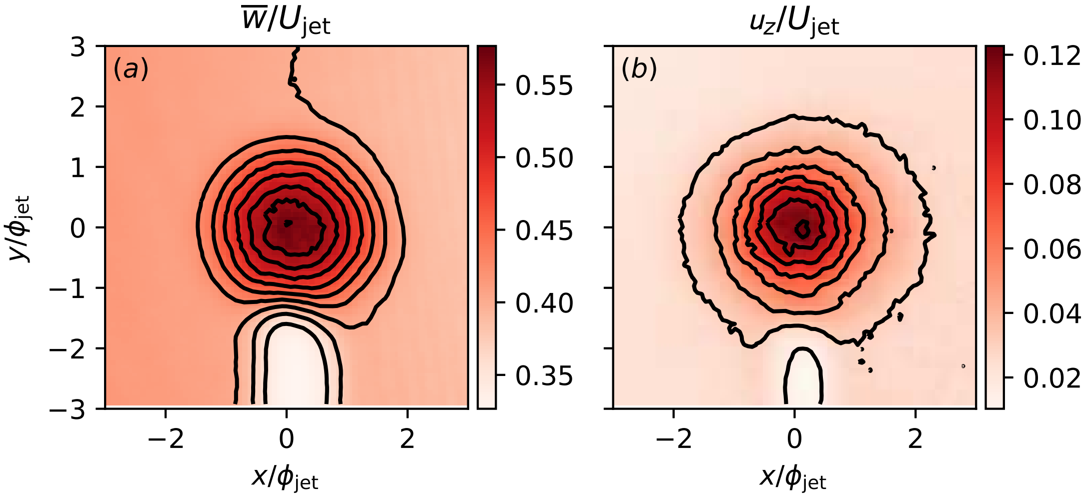

FIG. 5. PIV measurements of the mean and turbulence characteristics of the jet flow at $z/c = 1$. (a) streamwise component of the mean velocity $\bar{w}/U_{\mathrm{jet}}$, (b) turbulence intensity u_z/U_{jet}.

D. Jet entrainment by the vortex

The jet once released is entrained transversely by the wake vorticity as a function of the mutual jet–vortex spacing. In order to obtain a qualitative idea of this entrainment, we conducted additional PIV measurements (as described above), but by seeding the jet alone and not the rest of the incoming flow. This produces images of the jet exhaust identified by the seeding, while the surrounding is free of particles. Figure 6 shows the transverse distribution of the standard deviation of such images corresponding to the jet exhaust, at $z/c \in \{4, 20\}$ for the different jet–vortex configurations. The vortex and jet positions in the measurement plane are indicated by a cross and a circle, respectively. From Fig. 6, we observe at once that entrainment is enhanced upon reducing the distance between the jet and the vortex, in agreement with[8].

We see that for all jet–vortex configurations, the roll up of the vortex sheet issued at the wing trailing edge is centred around a location 5 % of the half span inward of the wing tip (marked by a cross). The trailing vortex is then subject to a gradual inward drift to at least 10 % of the half span at $z/c = 20$. Note that a detailed discussion of the vortex-centre motion follows in § IV. This latter vortex-centre position corresponds to the closest jet–vortex spacing of $d_{\mathrm{jet}}/b = 0.8$, chosen for this reason. The more distant jet positions $d_{\mathrm{jet}}/b \in \{0.44, 0.58\}$ are inward this location of the fully rolled-up vortex.

In the jet–vortex configuration with $d_{\mathrm{jet}}/b = 0.80$, the jet is wound up by the trailing vortex right after its release. At $z/c = 20$ the jet fills the entire domain of the vortex and its near periphery. In the second jet–vortex configuration with $d_{\text{jet}}/b = 0.58$, spiraling-up of the jet by the vortex is delayed and the core of the vortex is not populated significantly by the jet at $z/c = 20$. Lastly, in the jet–vortex configuration with $d_{\text{jet}}/b = 0.44$, the jet diffuses before significant entrainment into the vortex becomes possible and the absolute contamination of the core remains weak within the downstream range investigated.

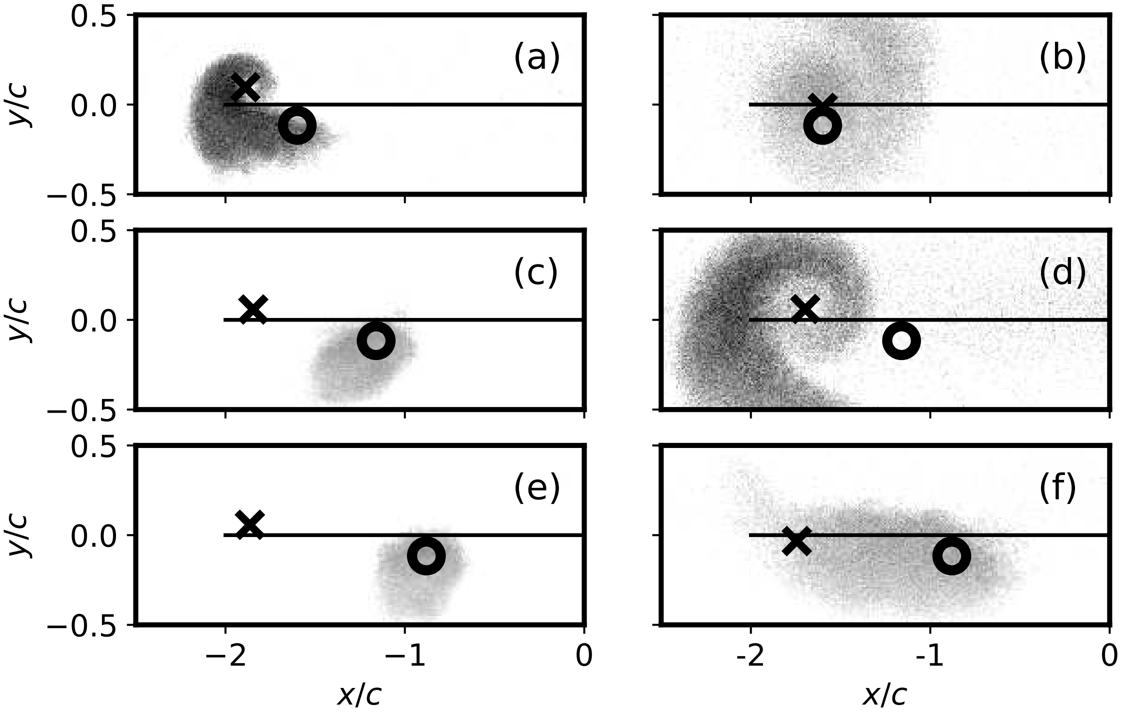

FIG. 6. Standard deviation of the spatial distribution of the seeding released at the jet in transverse planes at $z/c = 4$ (left column) and $z/c = 20$ (right column) for the various jet–vortex configurations. (a,b) $d_{\text{jet}}/b = 0.80$, (c,d) $d_{\text{jet}}/b = 0.58$, (e,f) $d_{\text{jet}}/b = 0.44$. The cross indicates the mean location of the vortex centre in the given measurement plane. The straight line indicates the trailing edge of the wing. The circle indicates the outflow section of the jet.

III. MEAN FLOW

A. Data analysis

Consider an Eulerian flow field $f(\boldsymbol{x}, z, t)$ which will be either one of the velocity components (u, v, w) or the thereof derived streamwise vorticity ω. Let M be one of the five measurement planes at $z = \text{const}$ in which we have measured $f(\boldsymbol{x}, z, t)$, $\boldsymbol{x} \in M$ over the time interval $(0, T)$. We assume $f(\boldsymbol{x}, z, t)$ to be a stationary random process (in t), while it may be non-homogeneous in z. By the ergodic hypothesis, time and ensemble averages can be identified and we define the mean as[23]

$$\overline{f}(\boldsymbol{x}, z) := \lim_{T\to\infty} \frac{1}{T} \int_0^T \mathrm{d}t \; f(\boldsymbol{x}, z, t). \tag{2}$$

The Reynolds decomposition then reads $f(\boldsymbol{x}, z, t) = \overline{f}(\boldsymbol{x}, z) + f'(\boldsymbol{x}, z, t)$ and we call f' the fluctuation.

In order to get meaningful vortex parameters, the measurement data has to be corrected for the effect of vortex displacement, usually attributed to the meandering phenomenon[24–27]. A discussion of the meandering motion is postponed to § IV A. This correction is straightforwardly implemented in the case of PIV measurements by means of a coordinate transformation into the reference frame following the vortex motion. That is, for $z = \text{const}$ we re-center the snapshots in the respective instantaneous vortex-centre position $f(\boldsymbol{x}, z, t) \leftarrow f(\boldsymbol{x} - \boldsymbol{X}(z, t), z, t)$ prior to taking averages[28]. Techniques for vortex identification are presented in[29]. Here, the vortex centre in the measurement plane at downstream position z is defined by the vector-valued process

$$\boldsymbol{X}(z, t) := \frac{1}{\Gamma_M} \iint_M \mathrm{d}\boldsymbol{x} \; \boldsymbol{x}\omega(\boldsymbol{x}, z, t), \; t \in (0, T) \tag{3}$$

in R^2.[30–32] The quantity Γ_M is the circulation, or the zeroth-order vorticity integral, defined around the contour ∂M bounding $M \subset R^2$ about the vortex. It is defined (applying Stokes' theorem) by the spatial vorticity integral[30,33]

$$\Gamma_M(z) := \iint_M \mathrm{d}\boldsymbol{x} \; \bar{\omega}(\boldsymbol{x}, z) \tag{4}$$

The circulation is a convenient measure for the strength of the vortex.

With no further information the variations of $\boldsymbol{X}(z, t)$ appear random, and thus the convenient way to account for it is to consider the leading stochastic moments, namely the mean and standard deviation

$$\overline{\boldsymbol{X}}(z) := \frac{1}{T} \int_0^T \mathrm{d}t \; \boldsymbol{X}(z, t) \quad \text{and} \quad \sigma^2_{X_i}(z) := \overline{(X_i(z, t) - \overline{X}_i(z))^2} \quad (i = 1, 2), \tag{5}$$

respectively.

Radial profiles are obtained by mapping the Cartesian x, y grid onto a polar mesh r, θ having its origin in the instantaneous vortex centre $\boldsymbol{X}(z, t)$. This coordinate transformation automatically corrects for the meandering motion. Assuming approximate homogeneity in the azimuthal coordinate, we can further average over $\theta \in (0, 2\pi)$.

All results shown in this section have been mapped to a polar mesh, averaged over the azimuthal coordinate and measurement time (cf., (2)). Eventually, the mean over the ten identically prepared runs is taken. In order to avoid overloading symbols, we denote this average with an overline as in (2) for convenience.

Very low values of the standard deviation between the ten identically prepared runs of the experiment indicates the repeatability of the experiments.

Due to the symmetries of the vortex flow, we can compute the radial profiles of the mean circulation as $\Gamma(r,z) = 2\pi r \bar{u}_\theta(r,z)$[31,34].

Given the radial profiles, several parameters can be defined to characterize the vortex. We define the vortex-core radius

$$r_1(z) := \underset{r\in(0,\infty)}{\arg\max}\ \bar{u}_\theta(r,z) \tag{6}$$

as the radial coordinate of the maximum of the mean azimuthal velocity. We make use of the convention to denote quantities evaluated at the core radius with a subscript $_1$; e.g., $\bar{u}_{\theta,1}(z) := \bar{u}_\theta(r_1,z)$ and $\Gamma_1(z) := \Gamma(r_1,z)$.

According to[35], we define the swirl number

$$q(z) := 1.57 \left| \frac{\bar{u}_{\theta,1}(z)}{\bar{u}_z(r=0,z) - \bar{u}_z(r\to\infty,z)} \right|, \tag{7}$$

whereas the mean streamwise velocity difference is relative to the free-stream velocity U_∞.

B. Experimental results

Before discussing the radial profiles of the mean vortex flow, it is illustrative to obtain a global impression of the whole wake flow. To this end, Fig. 7 shows the fluctuation kinetic energy u^2 normalized on the free-stream velocity squared U_∞^2 for the no-jet and jet–vortex $d_{\text{jet}}/b = 0.80$ configurations at $z/c = 2$ and $z/c = 20$, respectively. At the first measurement station, the no-jet wake is globally dominated by the vorticity sheet shed from the wing. The vorticity sheet is much less discernible in the $d_{\text{jet}}/b = 0.80$ jet–vortex configuration, as the dominating contribution comes from the jet flow, having about an order of magnitude larger fluctuation kinetic energy. In either configuration, we see that only the trailing vortex retains a discernible structure in the fluctuation kinetic energy by $z/c = 20$.

Figure 8 compares radial profiles of the mean azimuthal and streamwise velocity of the vortex in the no-jet and jet–vortex configuration with $d_{\text{jet}}/b = 0.80$ at the different measurement stations.

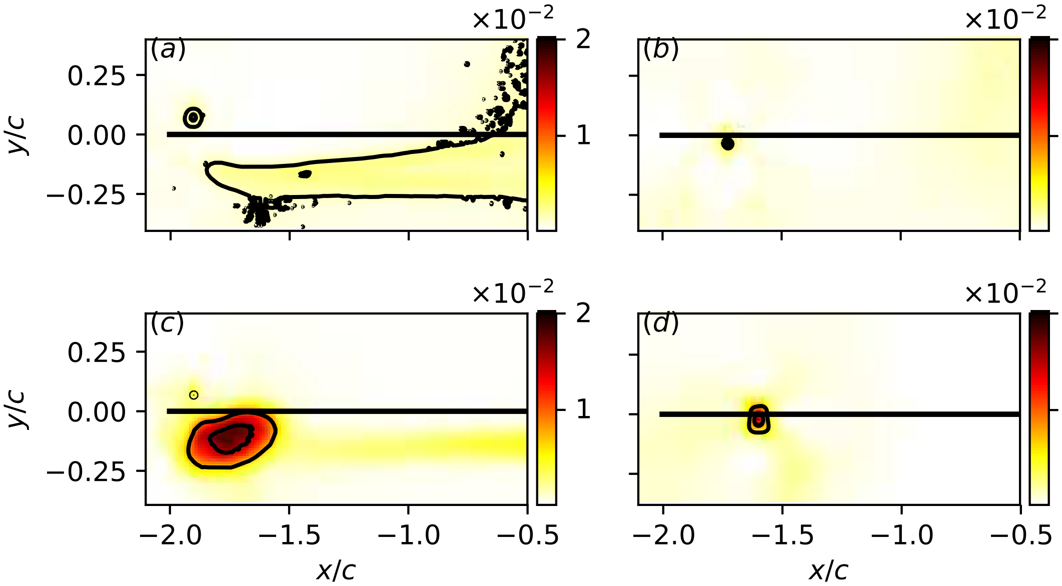

FIG. 7. Fluctuation kinetic energy u^2/U_∞^2. (a) no-jet configuration at $z/c = 2$, (b) no-jet configuration at $z/c = 20$, (c) jet–vortex configuration with $d_{\text{jet}}/b = 0.80$ at $z/c = 2$, (d) jet–vortex configuration with $d_{\text{jet}}/b = 0.80$ at $z/c = 20$. The black line illustrates the wing.

We observe the profiles to have qualitatively similar shapes in the two configurations and for all measurement planes. The streamwise mean vortex velocity is characterized by a wake-jet coexistence. That is, the wake-like behavior in the core turns into a jet-like flow in its periphery. Wake-like core flow is commonly observed in experiments[25,36,37]. This jet-wake characteristic is represented in the Moore–Saffman vortex[31] (further details can be found in Appendix A). Comparing Figs. 8*a* and *b*, we see that the coexistence gets much more pronounced in the jet–vortex configuration, likely as a consequence of the roll-up of the jet by the vortex. In all cases, the magnitude of the axial velocity increases downstream. The jet flow seems to have less structural effect on the azimuthal mean-velocity profiles, but strongly affects their maximum intensity.

These conclusions also hold true for the intermediate jet–vortex configurations $d_{\text{jet}}/b \in \{0.44, 0.58\}$ (not shown), which gradually transition between the two extrema shown in Fig. 8. While placing the jet at $d_{\text{jet}}/b = 0.44$ has almost no effect on the mean vortex flow over the considered measurement range, the intermediate spacing $d_{\text{jet}}/b = 0.58$ causes deviations from the no-jet reference mainly at the last measurement stations. Jet proximity promotes tangential velocity reduction, as is found for increased level of turbulence by[38]. The initial transition is likely a smooth function of d_{jet}, however, there seems to be a critical value $0.58 < d_{\text{jet}}/b < 0.80$ beyond which significant

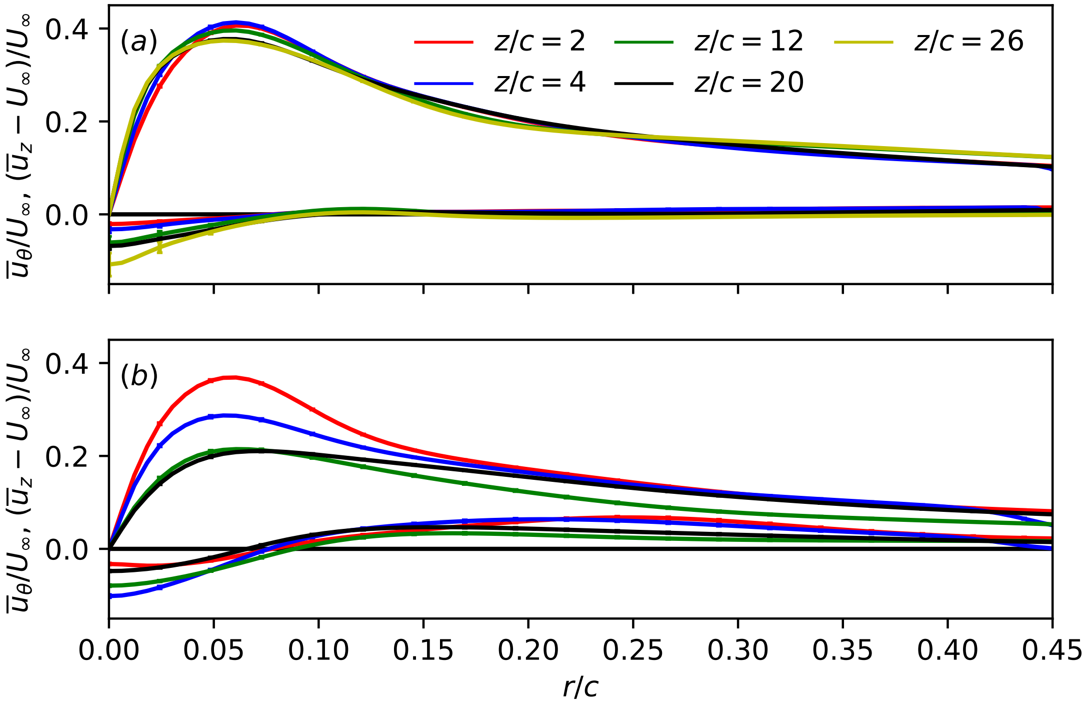

FIG. 8. Downstream evolution of the radial profiles of the streamwise and azimuthal mean velocity. (a) no-jet configuration, (b) jet–vortex configuration with $d_{\text{jet}}/b = 0.80$ spacing (no measurements were conducted at $z/c = 26$ in this configuration). The profiles are averaged over the ten runs at each measurement station and the error bars, defined as the standard deviation over the runs, indicate the variability between these runs.

differences in the mean flow are observed. Previous studies by[20,39] suggest this discontinuity in the dynamics to be related with entrainment of the jet in the vortex core already during roll up in the $d_{\text{jet}}/b = 0.80$ configuration, while it is not (or late) entrained in the other configurations. The azimuthal mean velocity asymptotically decays as $\sim r^{-n}$ with $n \approx 0.8 \pm 0.02$ in all configurations and measurement stations. (For comparison, elliptic loading corresponds to $n = 0.5$[31].) Slower than potential-vortex decay is characteristic of the Moore–Saffman vortex and the value of n in agreement with the findings of[34]. Section A details the comparison of the vortex profiles against the Moore–Saffman and Batchelor models.

These findings are supported by Fig. 9a, showing the downstream evolution of the maximum mean azimuthal velocity and streamwise mean velocity deficit in the core for all configurations. As stated above, the no-jet and $d_{\text{jet}}/b = 0.44$ configuration have very little difference over the considered measurement range and the $d_{\text{jet}}/b = 0.58$ configuration diverges mainly in the last measurement planes. Significantly different downstream evolution of the maxima is observed, however, in the $d_{\text{jet}}/b = 0.80$ configuration. We note that the streamwise velocity deficit is of the same magnitude in all cases and the effect of the vortex-superposed jet flow is mainly in the creation of an additional jet flow in the core periphery (cf., Fig. 8*b*). A little surprising, we observe a much stronger effect of the jet flow on the maximum of the azimuthal mean velocity which we find to decrease by about a factor two in the $d_{\text{jet}}/b = 0.80$ configuration over the measurement range. These general trends of decaying vortex mean-velocity maxima are analogous to experiments conducted in grid turbulence[26,28]. We find, however, that the vortex core radius remains at an essentially constant value of $r_1/c \approx 6 \times 10^{-2}$ over the measurement range and for all configurations, consistent with previous findings[20,25–27].

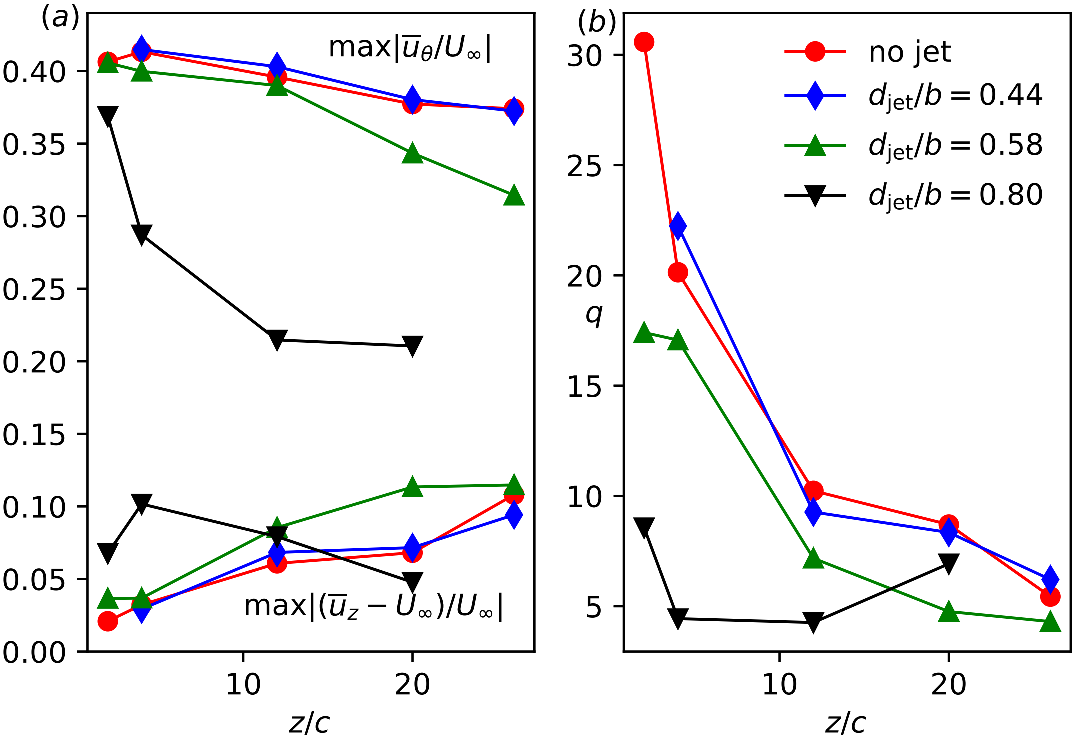

FIG. 9. Downstream evolution of the vortex parameters of the mean velocity in the different configurations. (*a*) maximum non-dimensional velocities, (*b*) swirl number q.

The information shown in Fig. 9*a* is readily combined into a single parameter, viz., the swirl number q defined in (7), that determines the local linear stability of the isolated Batchelor vortex. For values larger than about $q \approx 2.31$ the vortex is inviscidly stable to infinitesimal perturbations[40]. Viscous instabilities theoretically exist beyond this threshold for all q[41] but are presumably of no importance for the present study.

Figure 9*b* shows the downstream evolution of the mean swirl number for the different configurations. In agreement with the previous conclusions, the principal behavior is qualitatively similar in all cases but the closest $d_{\text{jet}}/b = 0.80$ spacing. Despite this latter configuration, decreasing maximium azimuthal velocity and increasing streamwise mean-velocity deficit combine to downstream-decreasing swirl numbers. However, over the considered measurement range the minimally attained values of about $q \approx 5$ remain well above the theoretical instability threshold. This suggests linear stability of the trailing vortex in all configurations. Albeit, particularly in the $d_{\text{jet}}/b = 0.80$ configuration the Batchelor vortex is a poor model as can be anticipated from Fig. 8*b*, showing a pronounced jet–wake coexistence in the vortex core. A more pertinent stability analysis should use the Moore–Saffman vortex as a base state. The only such analysis known to the authors, assuming an inviscid fluid, is due to[42]. Indeed, this study shows that the Moore–Saffman vortex gradually looses stability as it deviates from the Batchelor vortex and as long as the core is wake-like. That is, the unstable parameter range increases in $0.44 \leq n \leq 1$ and decreases again for $n < 0.44$. For $n = 0.8$,[42] report an instability threshold of $q = 1.7$, which is well below the swirl numbers $q \gtrsim 5$ in the experiment for all configurations (cf., Fig. 9*b*).

Figure 10 compares radial profiles of the mean circulation (4) of the vortex in the no-jet and jet–vortex configuration with $d_{\text{jet}}/b = 0.80$ at the different measurement stations. The circulation increases sharply within a distance approximately equal to $r_2 \approx 2r_1 \approx 0.1c$ in all configurations. This corresponds to the vortical zone associated with the vortex (cf., also[34]). The circulation shows continuous yet mild increments further outward this radius. The intermediate jet–vortex configurations (not shown) follow the same transition behavior as discussed in connection with Figs. 8 and 9. In the no-jet configuration, apart from the variation which is observed for $z/c \in \{12, 26\}$ away from the vortex, currently unexplained, the circulation profiles are practically constant over the entire downstream measurement range. This implies that the vortex roll up is completed within the first two chords behind the wing, consistent with[27,43,44].

On the other hand, the circulation profiles in the $d_{\text{jet}}/b = 0.80$ jet–vortex configuration show a distinct downstream evolution. Apart from the circulation at $z/c = 12$, the circulation profiles continuously broaden over a radial range restricted to approximately $r/c \lesssim 2\ldots 3r_1$. The asymptotic circulation $\Gamma(r \to \infty)$, however, seems to be almost unaffected and remains practically constant. This finding is in principal agreement with[34].

For a Lamb–Oseen vortex, the asymptotic circulation $\Gamma(r \to \infty)$ is identical to the initial value

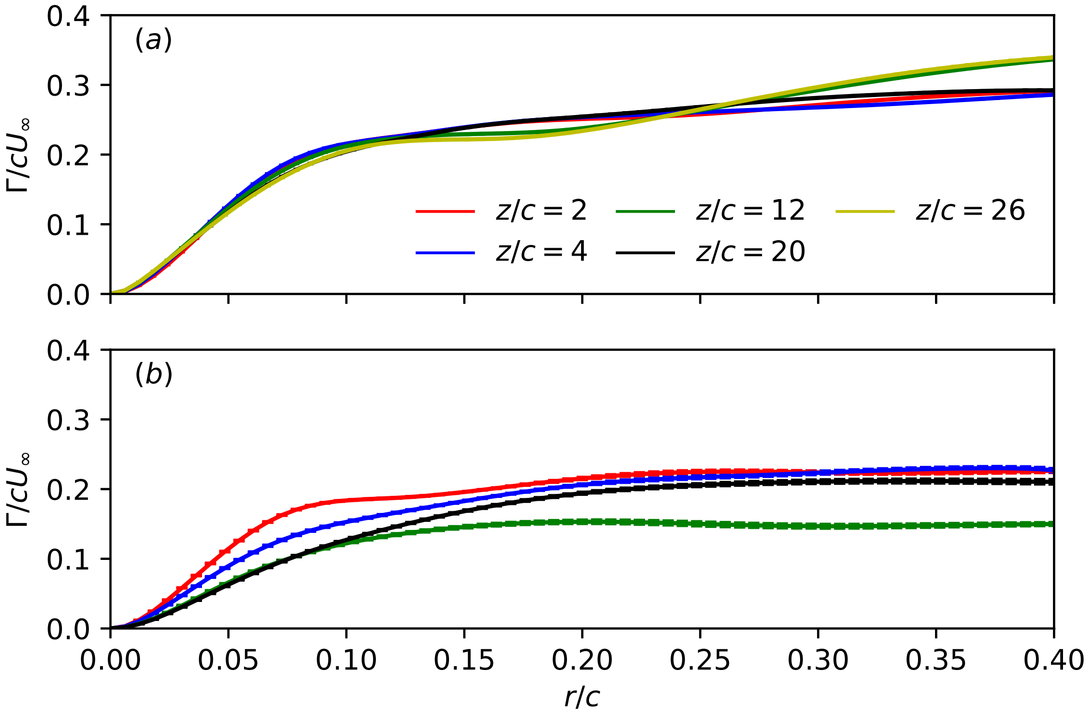

FIG. 10. Downstream evolution of the circulation. (a) no-jet configuration, (b) jet–vortex configuration with $d_{\mathrm{jet}}/b = 0.80$ spacing (no measurements were conducted at $z/c = 26$ in this configuration). The profiles are averaged over the ten runs at each measurement station and the error bars, defined as the standard deviation over the runs, indicate the variability between these runs.

Γ_0 and, hence, a convenient measure for the vortex strength. Assuming a Lamb–Oseen vortex, Γ_0 and the circulation at the core radius Γ_1 are related according to $\Gamma_0 = 1.397 \times \Gamma_1$[31]. Figure 11 shows the downstream evolution of Γ_1 for the different configurations. Taking an average value of $\Gamma_1/cU_\infty \approx 0.14$, we estimate $\Gamma_0/cU_\infty \approx 1.397 \times 0.14 \approx 0.20$. Comparing with Fig. 10 shows that $\Gamma_0 \approx \Gamma(r \to \infty)$. We thus define the circulation Reynolds number $R_\Gamma := \Gamma_0/\nu \approx 3 \times 10^4$. These values of the circulation are in agreement with previous studies[20,25,26,34].

IV. KINEMATICS AND DYNAMICS OF THE VORTEX

A. Vortex-centre motion

a. Lateral motion of the mean vortex centre. A pair of vortices exhibits a downward motion as a consequence of mutual Biot–Savart induction. We employ here a point vortex model of the

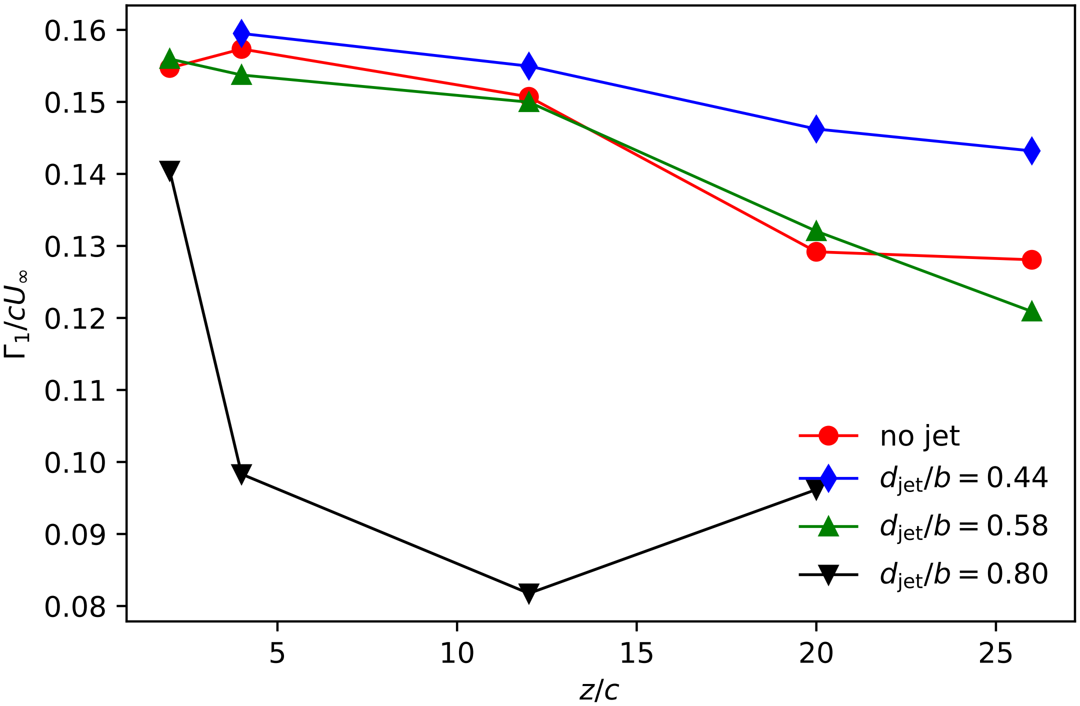

FIG. 11. Downstream evolution of the circulation at the core radius Γ_1 for the different configurations.

vortices to evaluate this trend. Such a model agrees with the fact that the separation of the two counter-rotating trailing vortices, which is of the order of the wing span $s \times b$ (cf., Fig. 12*a*) with $s \approx \pi/4$, is large compared to the vortex size r_2. A crude estimate yields $r_2/b \approx 2.5 \times 10^{-2}$. Using the point vortex model the translation velocity and trajectory are given by[33]

$$\frac{\dot{\overline{Y}}}{U_\infty} = -\frac{1}{U_\infty}\frac{2\Gamma_0}{\pi^2 b} \approx -0.01 \quad \rightarrow \quad \frac{\overline{Y}(z)}{c} = \frac{\overline{Y}_0}{c} - \frac{1}{U_\infty}\frac{2\Gamma_0}{\pi^2 b}\frac{z}{c} \approx 0.14 - 0.01\frac{z}{c}, \tag{8}$$

whereas $\Gamma_0/cU_\infty \approx 0.2$ denotes the circulation of each one of the trailing (point) vortices (cf., Fig. 10). Figure 12*b* shows the vertical downward translation of the mean vortex-centre location for the different configurations. Superposing the theoretical descent according to (8), assuming a fictitious origin at $\overline{Y}_0/c = 0.14$, we find acceptable agreement with the no-jet configuration in the last measurement planes.

If the idealization of point vortices was perfectly true, the conservation of momentum would imply that the spanwise separation between the two point vortices was preserved[32]. Figure 12*a* shows that in the experiment the vortices tend to converge monotonously towards the symmetry plane ($x = 0$).

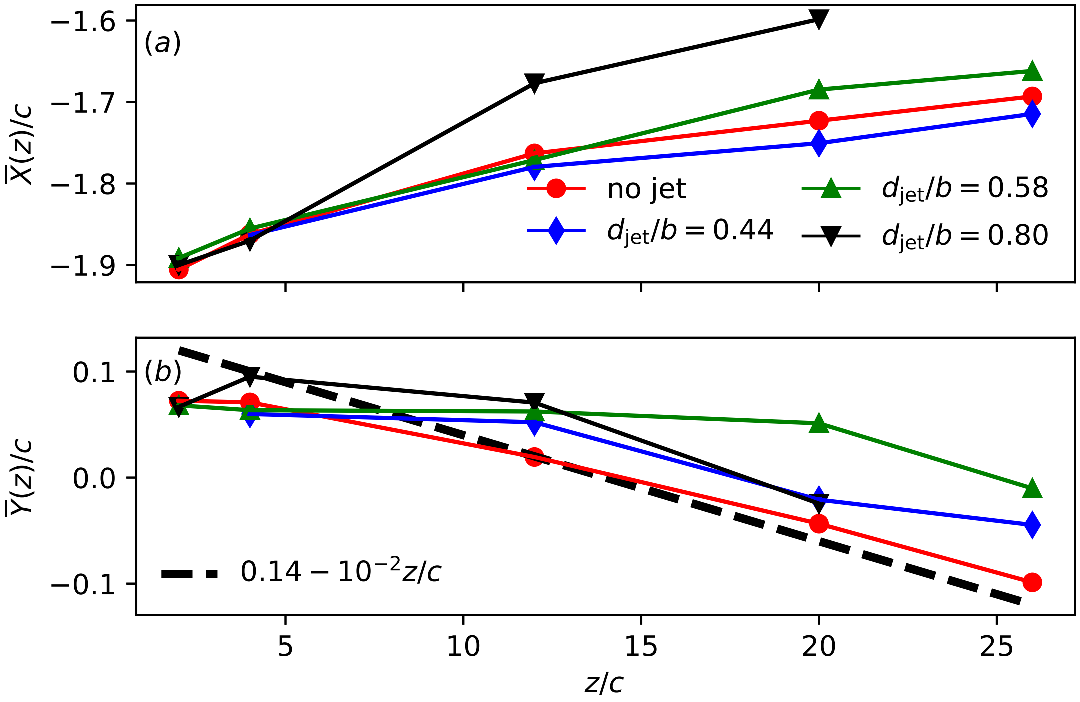

FIG. 12. Downstream evolution of the mean location of the vortex centre for the different configurations and comparison with the theoretical downward translation according to (8).

b. Vortex-centre fluctuation around the mean The displacement of the vortex and the effect of the jet are the most interesting features of the experiment. Figure 13 shows the growth of the two components of the vortex-centre standard deviation σ_{X_i}, (5), for the different configurations as a function of the downstream distance. The fact that $\sigma_X(z) \sim \sigma_Y(z)$ over the measurement range indicates that there is no preferred direction of the transverse motion of the vortex. We observe that the vortex-centre motion is a function of the mutual jet–vortex spacing. The jet effect remains low and progressive for $d_{\mathrm{jet}}/b \in \{0.44, 0.58\}$, however, for $d_{\mathrm{jet}}/b = 0.80$ the amplitude shows a steep initial increment, indicative of a changing mechanism of the jet–vortex interaction. In this last configuration, the amplitude increase is very rapid within the first $4-5$ chord lengths behind the wing and seems to saturate afterwards at a level approximately $3-4\%$ of c.

Downstream enhancing fluctuation levels of the vortex-centre motion is a generally observed phenomenon, usually referred to as meandering. An important feature of the meandering amplitude (defined as the standard deviation (5)) is its similarity with a diffusion dynamics, that was early on pointed out by[24]. The idea is that the vortices are essentially displaced as a Lagrangian object by the surrounding free-stream turbulence, which suggests an empirical law for the amplitude growth following

$$\frac{\sigma_{X_i}(z)}{c} = \sqrt{2\frac{\kappa}{cU_\infty}}\sqrt{\frac{z}{c}} \quad (i=1,2), \tag{9}$$

where κ denotes an eddy diffusivity.

A comparison of the square-root downstream growth predicted by the empirical meandering-amplitude scaling law (9) with the different configurations of the experiment is shown in Fig. 13. We find good agreement with $\sigma_{X_i}(z)/c = 10^{-3}\sqrt{z/c}$ downstream of $z/c = 4$ for the no-jet configuration. For comparison, identification of the eddy viscosity κ with the kinematic viscosity ν would lead to a slope prediction of $\sqrt{2\kappa/cU_\infty} \to \sqrt{2/R_c} \approx 10^{-5/2}$ with $R_c \approx 1.7\times 10^5$ in the experiment.

As expected from the above conclusions, the empirical law also closely corresponds to the jet–vortex $d_{\mathrm{jet}}/b = 0.44$ configuration. A significant divergence of the meandering amplitude from this law is, however, observed for the intermediate jet–vortex spacing of $d_{\mathrm{jet}}/b = 0.58$. Still, the experimental result reasonably follows an amplitude scaling law of the form (9) if the eddy-viscosity parameter is adjusted appropriately. Unlike these three cases, the meandering amplitude in the $d_{\mathrm{jet}}/b = 0.80$ configuration is qualitatively different from the empirical law (9). We note that the vortex response in this last configuration is reminiscent of the findings of[12], although, in their experiment, the synthetic jet was blowing perpendicular to the trailing vortex at the wing tip. Our findings suggest that the meandering dynamics is actually qualitatively the same in the no-jet and jet–vortex configurations with $d_{\mathrm{jet}}/b \in \{0.44, 0.58\}$ (differences are only in terms of the magnitude), while the dynamics is qualitatively and quantitatively different for the closest jet–vortex spacing of $d_{\mathrm{jet}}/b = 0.80$.

In agreement with[24], this finding strongly suggests that vortex meandering is the consequence of the forcing by disturbances located *outside* of the vortex. Even more, the dependence on the relative spacing d_{jet} indicates the existence of a preferred location for optimal excitation. We recall from the previous study of[20] that the jet flow does not entrain into the vortex core for $d_{\mathrm{jet}}/b \in \{0.44, 0.58\}$ (over the measurement range). This suggests that the effect of the jet on the vortex to be not principally different from that of an enhanced free-stream turbulence intensity, e.g., due to grid turbulence. Indeed, experiments on vortex meandering in grid turbulence support this conclusion[24,34,45].

The previous section § IV A indicates how the kinematics of the vortex is dominated by a continuous and increasing lateral motion on top of a mean downward movement. The dynamics

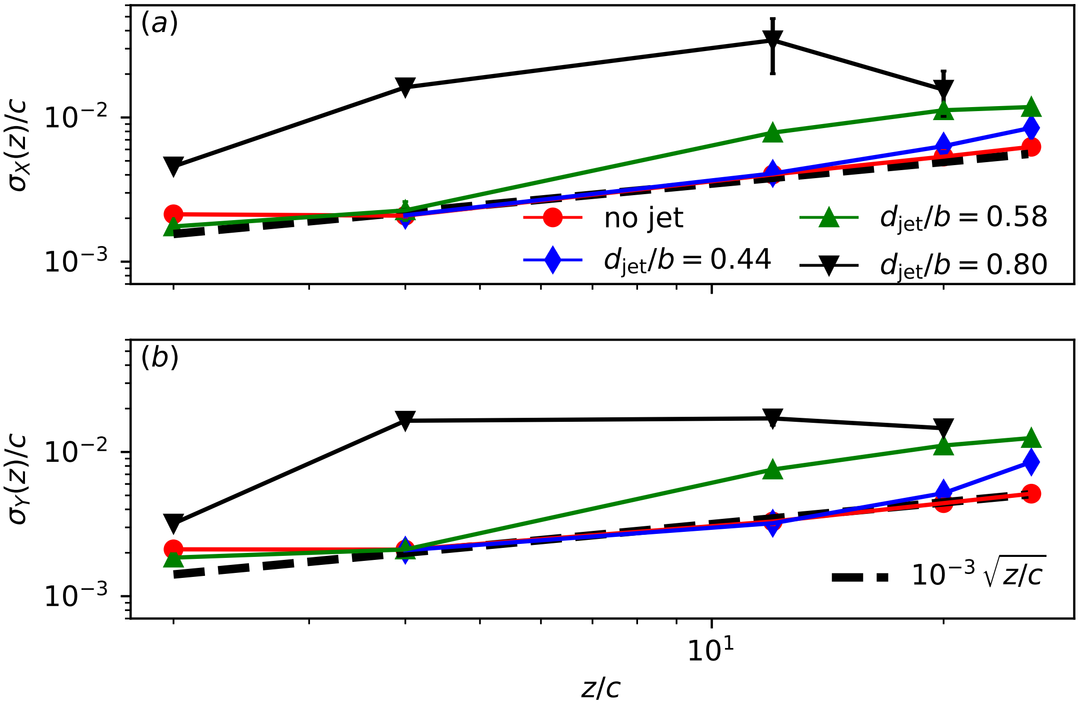

FIG. 13. Double-logarithmic representation of the downstream evolution of the meandering amplitude (5) for the different configurations and comparison with the scaling law (9).

of the vortex is now analyzed through the second-order statistic moments of the velocity field, namely Reynolds stresses and proper orthogonal decomposition (POD).

B. Reynolds stresses

Let $z/c \in \{4, 20\}$ and $\boldsymbol{x} \in M$. We define the second central stochastic moment in each space point

$$R_{ij}(\boldsymbol{x}, z) = \overline{u'_i(\boldsymbol{x}, z) u'_j(\boldsymbol{x}, z)} \quad (i, j = 1, 2, 3), \tag{10}$$

conveniently referred to as Reynolds stresses. Reynolds stresses received not much attention in previous experiments on trailing vortices. Besides the seminal work by[46], Reynolds stresses have been computed by[26,28,36].

A comparison of the Reynolds stresses (10) in the no-jet and jet–vortex configuration with $d_{\mathrm{jet}}/b = 0.80$ is shown in Figs. 14–17 for the measurement planes located at $z/c \in \{4, 20\}$. Analogously to our previous remarks, the intermediate jet–vortex configurations continuously transition between these two extrema.

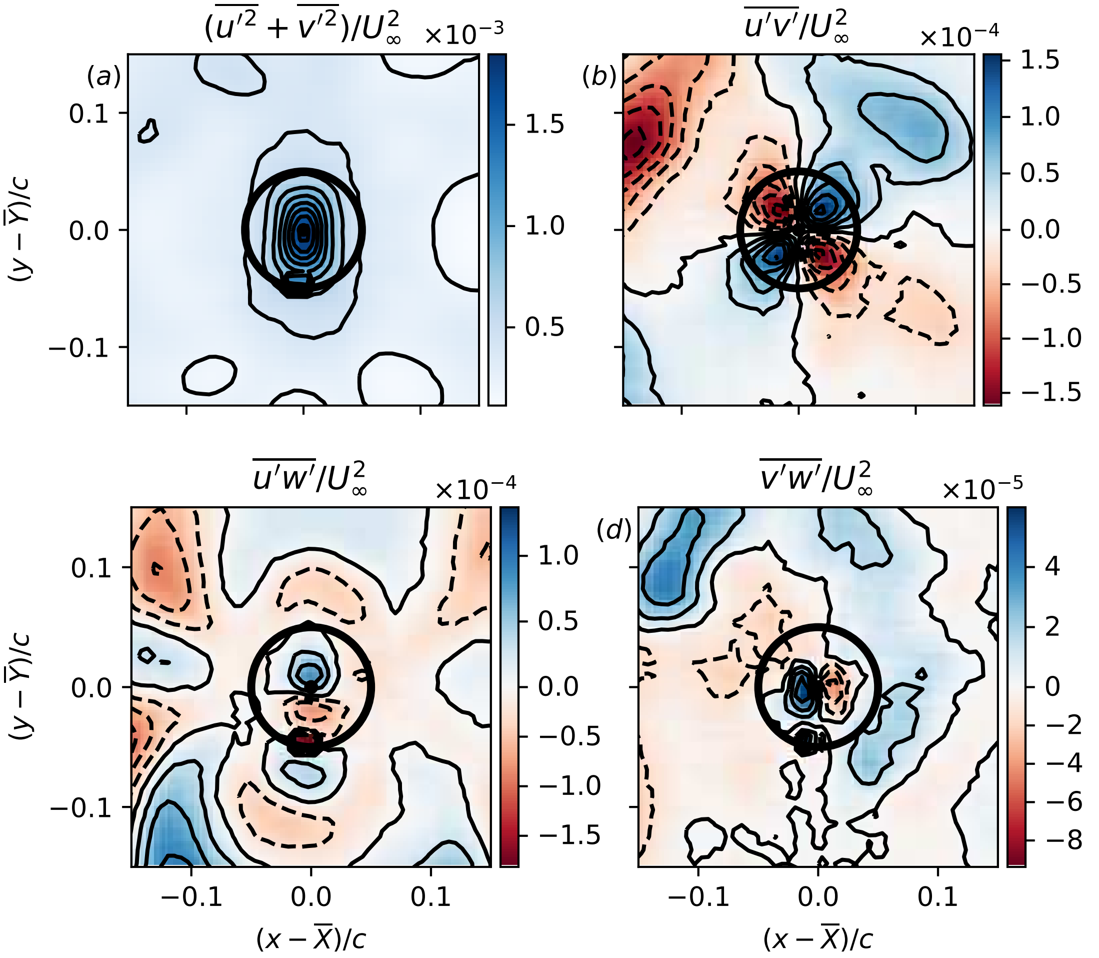

FIG. 14. Reynolds stresses at $z/c = 4$ in the no-jet configuration. (a) transversal fluctuation kinetic energy $(\overline{u'^2}+\overline{v'^2})/U_\infty^2$, (b) spanwise-vertical $\overline{u'v'}/U_\infty^2$, (c) spanwise-streamwise $\overline{u'w'}/U_\infty^2$, (d) vertical-streamwise $\overline{v'w'}/U_\infty^2$. The solid circle of radius $r_1/c = 6\times10^{-2}$ and black dot indicate the vortex core and mean centre, respectively.

We find the fluctuation kinetic energy to have mainly contributions from the transversal components $R_{11}+R_{22} = (\overline{u'^2}+\overline{v'^2})/U_\infty^2$, which are shown in the respective top-left Figs. 14*a*–17*a*. The contribution from the streamwise fluctuation kinetic energy $R_{33} = \overline{w'^2}/U_\infty^2$ is at least about an order of magnitude less in all but the $d_{\text{jet}}/b = 0.80$ jet–vortex configuration, viz., $\overline{u'^2} \sim \overline{v'^2} \gg \overline{w'^2}$. This suggests that the energy-carrying vortex modes are associated with transversal rather than longitudinal motion. We further observe from Figs. 14*a*–17*a* that the fluctuation kinetic energy is approximately axisymmetric and essentially confined to the vortex core (indicated by a bold black circle of radius r_1). Although this confinement already applies at the first measurement sta-

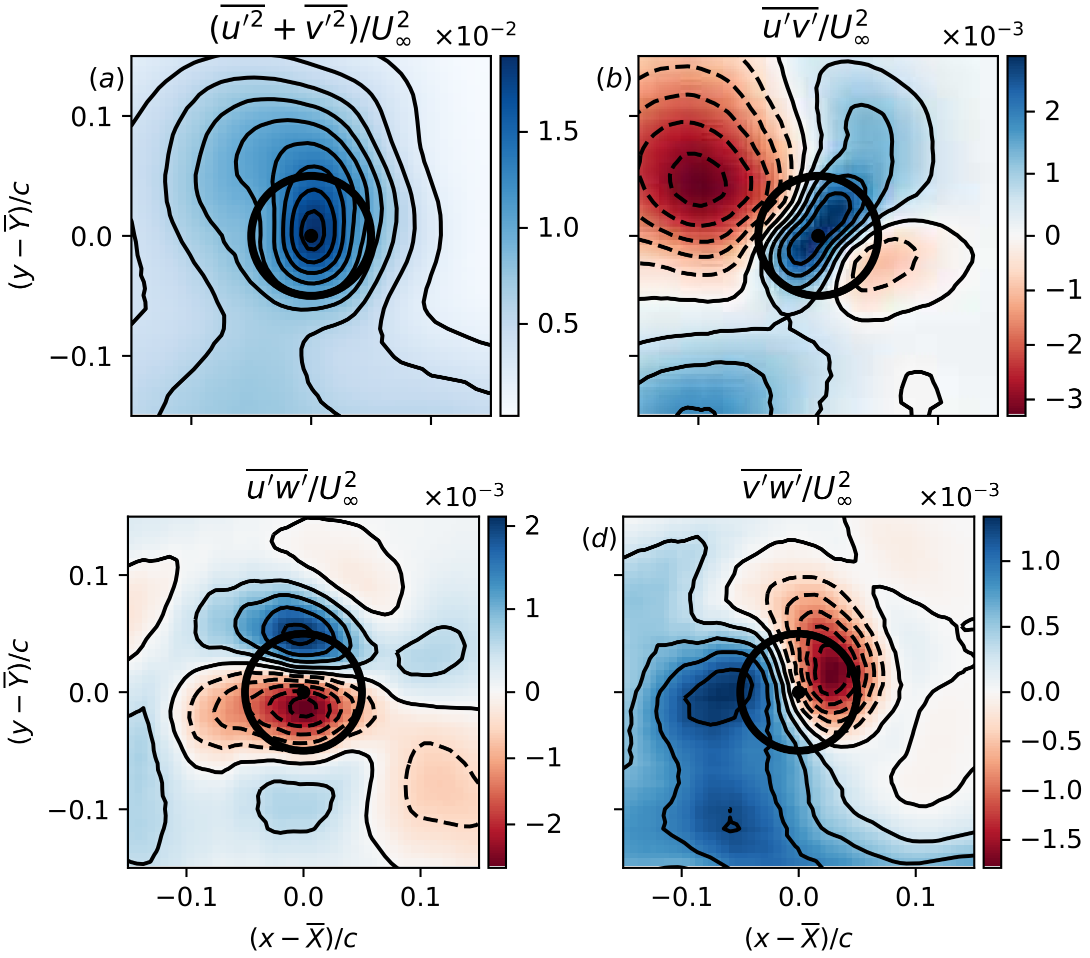

FIG. 15. Reynolds stresses at $z/c = 4$ in the jet–vortex configuration with $d_{\mathrm{jet}}/b = 0.80$ spacing. (a) transversal fluctuation kinetic energy $(\overline{u'^2}+\overline{v'^2})/U_\infty^2$, (b) spanwise-vertical $\overline{u'v'}/U_\infty^2$, (c) spanwise-streamwise $\overline{u'w'}/U_\infty^2$, (d) vertical-streamwise $\overline{v'w'}/U_\infty^2$. The solid circle of radius $r_1/c = 6\times10^{-2}$ and black dot indicate the vortex core and mean centre, respectively.

tions, it becomes gradually more pronounced and sharper as we move downstream. Eventually, we observe that the transversal fluctuation kinetic energy $R_{11}+R_{22}$ in the no-jet configuration amplifies by about almost an order of magnitude over the measurement downstream range, while the streamwise component $\overline{w'^2}$ remains at a nearly constant level (not shown). This also holds for the $d_{\mathrm{jet}}/b = 0.44$ configuration, whereas $\overline{w'^2}$ is amplified by the same factor of ten in the $d_{\mathrm{jet}}/b = 0.58$ configuration (not shown). It remains, however, an order of magnitude less than the transversal fluctuation kinetic energy. Again the downstream evolution in the $d_{\mathrm{jet}}/b = 0.80$ configuration is qualitatively different in that all fluctuation kinetic energies are of similar order, remaining ap-

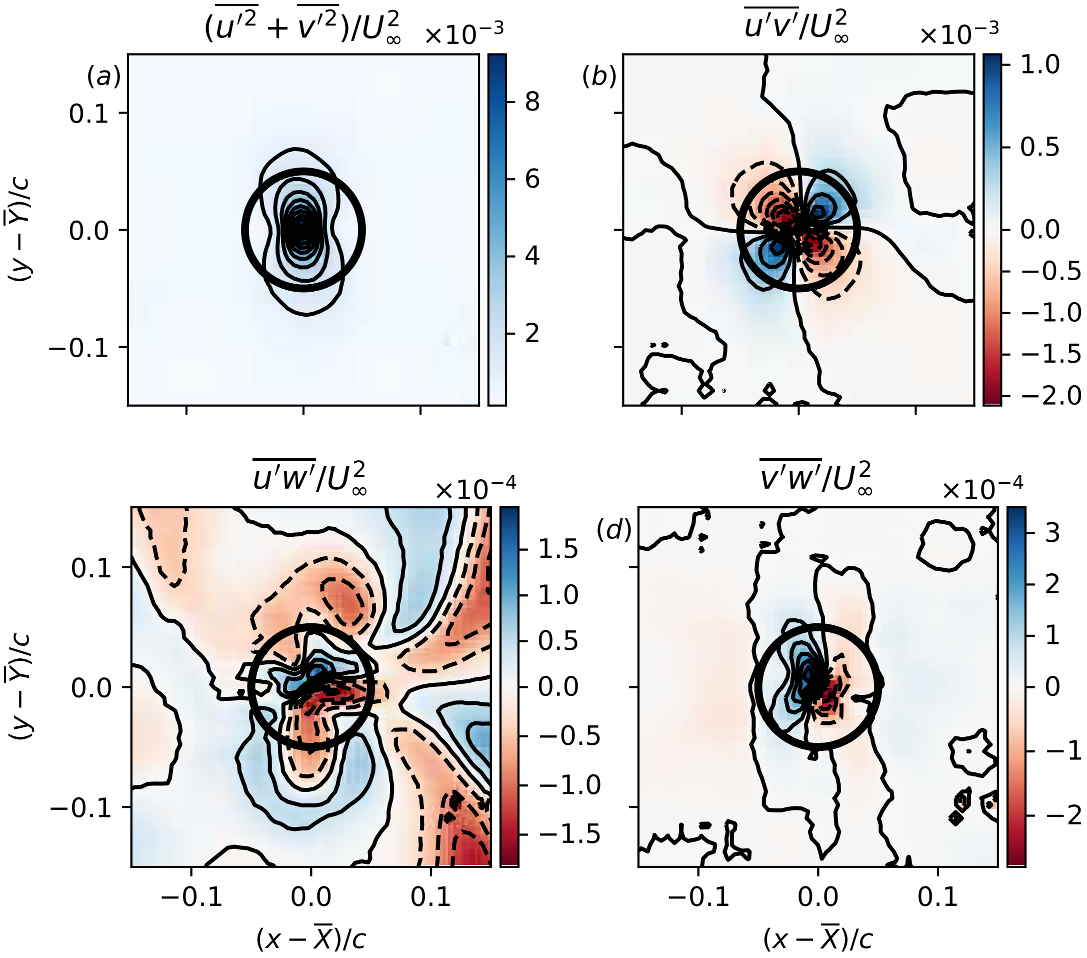

FIG. 16. Reynolds stresses at $z/c=20$ in the no-jet configuration. (a) transversal fluctuation kinetic energy $(\overline{u'^2}+\overline{v'^2})/U_\infty^2$, (b) spanwise-vertical $\overline{u'v'}/U_\infty^2$, (c) spanwise-streamwise $\overline{u'w'}/U_\infty^2$, (d) vertical-streamwise $\overline{v'w'}/U_\infty^2$. The solid circle of radius $r_1/c=6\times10^{-2}$ and black dot indicate the vortex core and mean centre, respectively.

proximately constant over the measurement range.

As of the relative magnitudes, similar trends hold for the remaining Reynolds stresses. The dominant contribution comes from the transversal stress $R_{12}=\overline{u'v'}/U_\infty^2$ in all the configurations (Figs. 14*b* and 16*b*), with an amplification of about an order of magnitude, except for $d_{\text{jet}}/b=0.80$. Again, the two Reynolds stresses involving the streamwise fluctuation velocity, $R_{13}=\overline{u'w'}/U_\infty^2$ (Figs. 14*c* and 16*c*) and $R_{23}=\overline{v'w'}/U_\infty^2$ (Figs. 14*d* and 16*d*), have much less discernible spatial structure and remain at an approximately constant level. We note that the sharp four-lobed spatial pattern at $z/c=20$ is already present at $z/c=4$, although less sharp and accompanied by

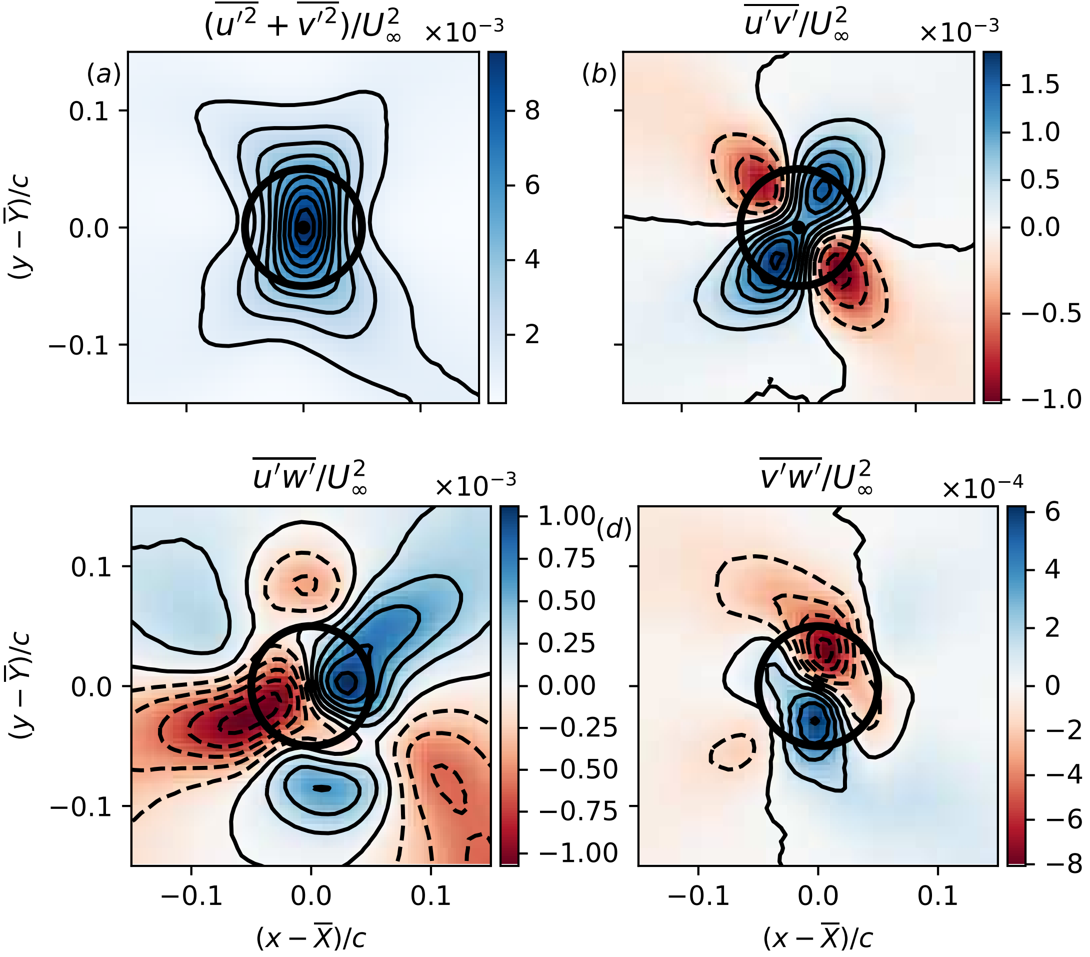

FIG. 17. Reynolds stresses at $z/c = 20$ in the jet–vortex configuration with $d_{\text{jet}}/b = 0.80$ spacing. (a) transversal fluctuation kinetic energy $(\overline{u'^2}+\overline{v'^2})/U_\infty^2$, (b) spanwise-vertical $\overline{u'v'}/U_\infty^2$, (c) spanwise-streamwise $\overline{u'w'}/U_\infty^2$, (d) vertical-streamwise $\overline{v'w'}/U_\infty^2$. The solid circle of radius $r_1/c = 6\times10^{-2}$ and black dot indicate the vortex core and mean centre, respectively.

significant contribution in the core periphery.

The Reynolds stresses in the $d_{\text{jet}}/b = 0.80$ configuration are associated with qualitatively similar spatial patterns. However, the patterns are less confined to the core, having a broader, stronger and sharper pattern already at $z/c = 4$. It is remarkable that, besides being less confined, the vortex develops the same Reynolds stress patterns by $z/c = 20$ in all configurations.

C. Proper orthogonal decomposition

a. Background The proper orthogonal decomposition (POD) is the optimal representation of a stochastic function with respect to the L^2-norm, i.e., in terms of the variance contained in a truncated representation[47]. Note that the following analysis always assumes measurements being taken in one plane $z = \text{const.}$ so, for readability, we suppress explicit dependence.

Let the Eulerian fluctuation field, after Reynolds decomposition, $t \mapsto f'(\boldsymbol{x},t) \in L^2(M)$ be a stationary random process (cf., § III). The proper-orthogonal decomposition theorem[47] then guarantees existence of the expansion

$$f'(\boldsymbol{x},t) = \sum_{l=1}^{\infty} a_l(t)\phi_l(\boldsymbol{x}) \quad \forall t \in (0,T),\ \boldsymbol{x} \in M \tag{11}$$

such that (an asterisk denoting complex conjugation)

$$\overline{a_k a_l^*} = \lambda_l \delta_{kl} \quad \text{and} \quad \iint_M \mathrm{d}\boldsymbol{x}\ \phi_k(\boldsymbol{x})\phi_l^*(\boldsymbol{x}) = \delta_{kl} \quad \forall k,l = 1,2,\ldots,\infty \tag{12}$$

if and only if

$$\iint_M \mathrm{d}\boldsymbol{x}'\ \overline{f'(\boldsymbol{x})f'^*(\boldsymbol{x}')}\phi(\boldsymbol{x}') = \lambda\phi(\boldsymbol{x}) \quad \forall \boldsymbol{x} \in M. \tag{13}$$

We note that (11) constitutes an expansion of the random function f' into a deterministic basis $\operatorname{span}\{\phi_l\} \subset L^2(M)$ of the linear manifold f' and random expansion coefficients $t \mapsto a_l(t)$. The expansion coefficients are defined by the $L^2(M)$-projection $a_l(t) := \iint_M \mathrm{d}\boldsymbol{x}\ \phi_l(\boldsymbol{x}) f'^*(t,\boldsymbol{x})$.

In practice, we compute the proper orthogonal decomposition using the method of snapshots[47,48]. For this purpose, we note that the actual measurement of the continuous random field yields a discrete sample on the spatio-temporal grid of dimension $K \times N$, where K and N are the number of spatial and temporal measurement points in every measurement plane, respectively. As usual, we call N the number of snapshots and the $R^{K\times N}$-matrix $\boldsymbol{F} := (\boldsymbol{f}^1, \boldsymbol{f}^2, \ldots, \boldsymbol{f}^N)$, $\boldsymbol{f}^q = \boldsymbol{f}((q-1)\Delta t) \in R^K$ for $q = 1,2,\ldots,N$, the snapshot matrix. The sampling interval Δt is of the order of the correlation time or larger[48], which guarantees approximate independence of subsequent snapshots[23]. Under these conditions, the above proper orthogonal decomposition is equivalent to solving the reduced eigenvalue problem

$$\frac{1}{N}\sum_{p=1}^{N} (\boldsymbol{f}^q, \boldsymbol{f}^p) b_p = \lambda b_q \quad \forall q = 1,2,\ldots,N \tag{14}$$

with $(\cdot,\cdot)$ a (weighted) inner product in R^K approximating the inner product (12) in $L^2(M)$. The expansion of the eigenvalues in (13) result from $\phi = \sum_{q=1}^{N} b_q \boldsymbol{f}^q$.

b. POD results. The previous analysis of Reynolds stresses reveals the governing contribution to the vortex fluctuation by the transversal components. The transversal dynamics are conveniently combined into a scalar field as the streamwise vorticity. We therefore computed the POD of the fluctuation streamwise vorticity ω', in order to characterize the main contributions to the variance of the transversal motion. Previous POD analysis of vortex-dominated flow have been done on the vorticity[44,49,50] as well as on the velocity[12,37].

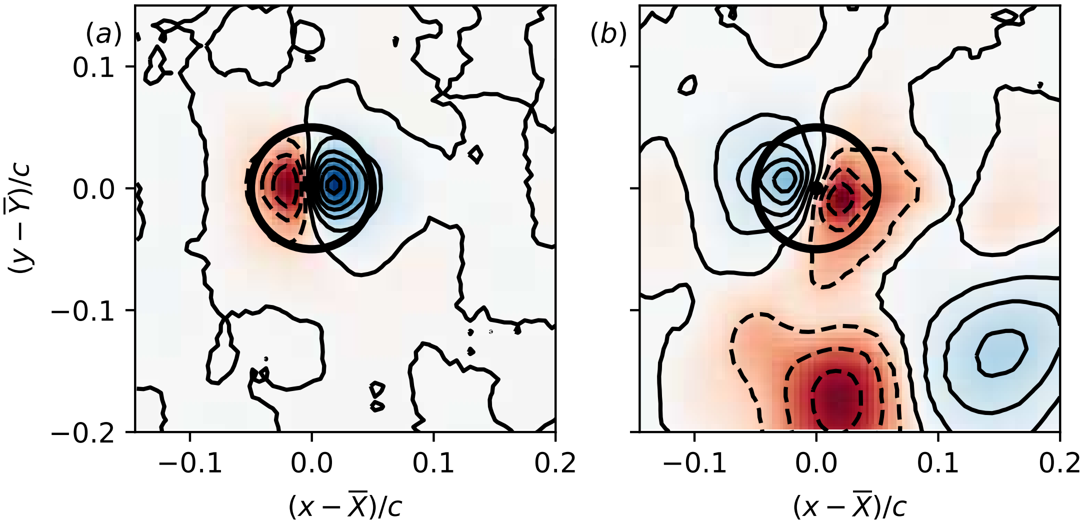

FIG. 18. Leading POD mode of the streamwise fluctuation vorticity in the first measurement plane at $z/c = 2$. (*a*) no-jet configuration, (*b*) jet–vortex configuration with $d_{\text{jet}}/b = 0.80$. Blue (red) color shading and solid (dashed) contours represent positive (negative) values with an arbitrary and not identical scaling. The solid circle of radius $r_1/c = 6\times10^{-2}$ and black dot indicate the vortex core and mean centre, respectively.

A comparison of the leading POD mode in the no-jet and $d_{\text{jet}}/b = 0.80$ jet–vortex configuration are shown in Figs. 18 and 19 for $z/c = 2$ and $z/c = 20$, respectively. We recognize the well-known dipolar vorticity pattern confined to the vortex core (indicated by a bold black circle) associated with a displacement wave. The second POD mode is structurally identical but mutually rotated by 90°, while the higher-order modes constitute multi-polar patterns of continuously increasing complexity (not shown) . These results are in agreement with previous experiments, e.g.[44,49,50]. The leading POD modes of the intermediate jet–vortex configurations transition continuously between the patterns shown in Figs. 18 and 19.

At the first measurement station $z/c = 2$, additional to the typical dipolar vortex response mode, the leading POD mode in the $d_{\text{jet}}/b = 0.80$ jet–vortex configuration contains an important mark

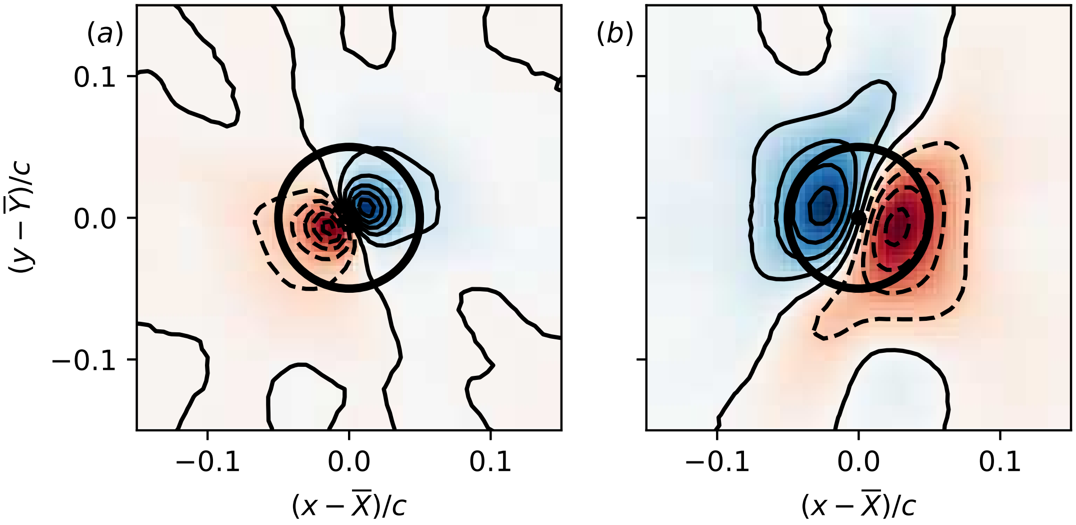

FIG. 19. Leading POD mode of the streamwise fluctuation vorticity in the first measurement plane at $z/c = 20$. (*a*) no-jet configuration, (*b*) jet–vortex configuration with $d_{\mathrm{jet}}/b = 0.80$. Blue (red) color shading and solid (dashed) contours represent positive (negative) values with an arbitrary and not identical scaling. The solid circle of radius $r_1/c = 6 \times 10^{-2}$ and black dot indicate the vortex core and mean centre, respectively.

of the jet flow outside the vortex core, which disappears by $z/c = 4$. From $z/c = 4$ on, the leading dipolar POD modes in all configurations remain essentially structurally unchanged, while contributions in the free stream gradually disappear. Recalling the definition of the vortex centre (3), the greater lateral extent of the leading POD modes upon increasing d_{jet} (the jets closer to the wing tips) explains the observed larger lateral motion amplitudes in Fig. 13.

The downstream evolution of the absolute POD eigenvalue (normalized on c^2/U_∞^2) associated with the leading POD mode is compared for the different configurations in Fig. 20*a*. This result is reminiscent of the analysis in[12].

It is instructive to compare the evolution of the absolute eigenvalue (in Fig. 20*a*) with that of the relative share the leading eigenvalue has in the total variance, i.e., $\lambda_1/\sum_{j=1}^{N}\lambda_j$. This is shown in Fig. 20*b*. We see that in this case the downstream evolution in the different configurations approximately collapse. Keeping in mind that the absolute values increase with d_{jet} (cf., Fig. 13*a*), this suggests that the jet tends to excite a wider range of vortex response modes and that this range becomes larger the smaller the relative jet–vortex spacing is. We support this conclusion by considering the POD eigenvalue spectra (of the first ten eigenvalues) for the different configurations in Fig. 21. While we see the almost exclusive excitation of the leading dipolar POD-mode pair in

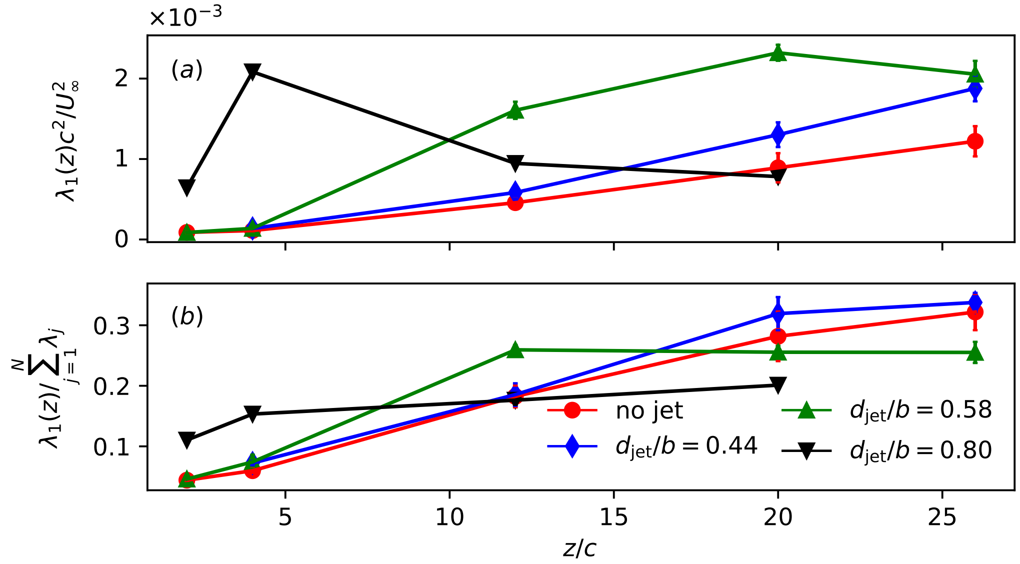

FIG. 20. Downstream evolution of the leading eigenvalue of the POD of the fluctuation vorticity for the different jet–vortex interaction configurations. (*a*) absolute value normalized on $c^2 U_0^{-2}$ as in Fig. 21. (*b*) relative contribution of the modal variance with respect to the total variance level in the respective measurement planes. Small markers are the results for the individual runs, while the respective bold markers (connected by solid lines) are the mean over all runs.

the no-jet configuration (Fig. 21*a*), progressively more POD modes are amplified downstream as we increase the jet separation distance d_{jet}.

V. CONCLUSION

We presented a wind-tunnel experiment on jet–vortex interaction for variable relative spacing d_{jet} using PIV measurements and a generic apparatus mimicking cruise flight, made of an inclined rectangular wing equipped with two jets underneath. The strength of the jet flow was designed to be realistic for the given setting and was kept the same throughout the different configurations. Despite completing previous experimental studies (e.g.,[20]), the present analysis, providing all the inflow conditions, in particular that for the jet exhaust, constitutes a complete and unique data set to calibrate simulation tools.

Our focus was on the vortex-response characteristics as a function of the different jet positions $d_{\mathrm{jet}}/b \in \{0.44, 0.58, 0.80\}$. The wake flow comprises the trailing vortices that form near the wing

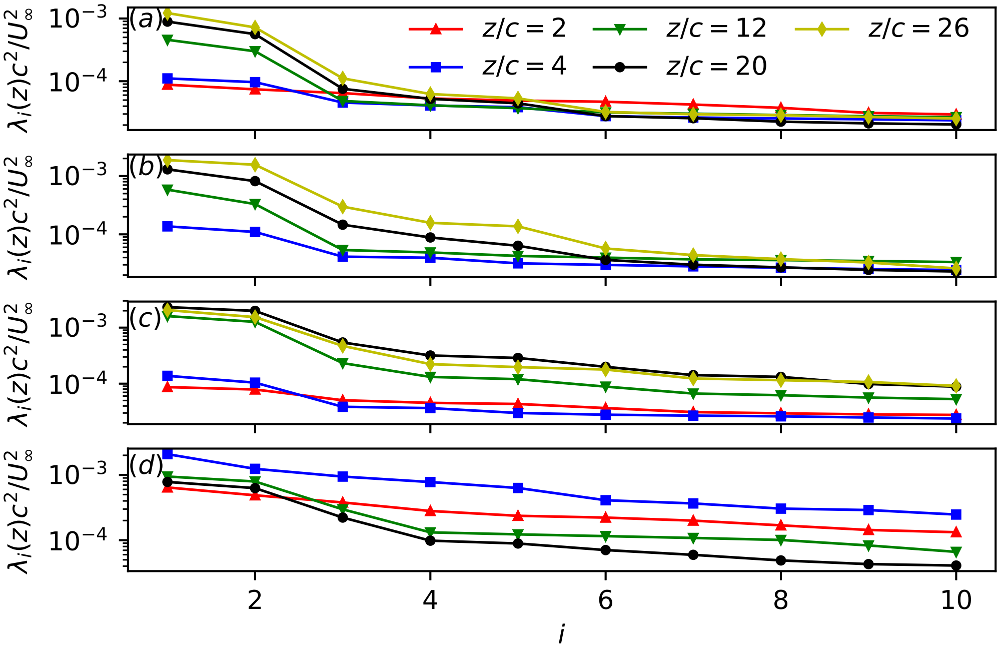

FIG. 21. Eigenvalue (mean over all runs) spectra of the largest ten values from POD of the vorticity covariance for the different configurations and measurement stations. (a) no-jet configuration, (b) jet placement $d_{\text{jet}}/b = 0.28$, (c) jet placement $d_{\text{jet}}/b = 0.21$, (d) jet placement $d_{\text{jet}}/b = 0.10$. The different measurement stations (see legend in (a)) are shown with the same marker style and color in each configuration.

tips, the rolling-up vortex sheet issued at the wing trailing edge and the jets for all but the no–jet configurations. The vortices are found to roll-up within the first two chords behind the wing and to descend under the mutual induction. Their circulation is little influenced by the jet presence and reaches approximately the value $0.2cU_\infty$. The vortex mean velocity profiles exhibit a close to Gaussian evolution for the azimuthal velocity, while the streamwise mean velocity yields a velocity deficit in the core and a local jet-like overshoot in the core periphery, where the jets are present and entrained, all the more so as the jets are initially located closer to the tips. We show that the no-jet configuration agrees reasonably well with the Batchelor model, while the jet–vortex configurations follow the Moore–Saffman model with an n-parameter roughly equal to 0.8.

The most interesting and largely novel result of the experiment is the persistent and strong unsteady lateral motion of the vortex that is found for all configurations, with increased amplitude as a function of the jets' presence and proximity to the wing tips. The statistical analyses of the leading-order stochastic moments revealed several key conclusions. Namely, (i) the motion of the vortices shows no preferred direction within the downstream range of the measurement; (*ii*) the motion amplitude follows a diffusion-like law in the downstream direction that suggests a similarity of our observations with many other experiments and what is referred to as vortex meandering. Lastly, (*iii*) the closest jet–vortex configuration, with $d_{jet}/b = 0.8$, departs from this general behavior by seemingly disrupting the vortices right after their formation close to the trailing edge, and setting a sudden large amplitude of motion. This discontinuous and qualitatively different vortex response upon reducing the mutual jet–vortex spacing beyond a certain point has been reported for the first time.

All governing parameters other than the free-stream turbulence intensity remaining unchanged points towards the net disturbing influence of the jets as a function of d_{jet}. This vortex-response characteristic suggests that a preferred external excitation location r_c exists. Taking the inward shift of the vortex into consideration, this location can be estimated to be $6 < r_c/r_1 \lesssim 12$. In particular, this result suggests that vortex meandering is neither due to a linear vortex instability exclusively present in the core, nor the consequence of a confining effect of the facility walls. Rather, we have evidence that meandering is in fact the vortex response to disturbances of a generic nature situated in the near periphery of the core. It is noteworthy that this conclusion is consistent with the results of recent receptivity studies by [51,52]. The pertinence of these and related studies (e.g.,[53]) to explain experimental vortex dynamics is emphasized by the evidence for a linear vortex dynamics implied by our results. Although not conclusive, these conclusions contribute important novel aspects on the question of the origin and nature of unsteady vortex dynamics.

The vortex tends to concentrate practically all the fluctuation kinetic energy in the core which is amplified downstream in all but the $d_{\mathrm{jet}}/b = 0.80$ configuration and the main contribution to the Reynolds stresses comes from the transversal components. Based on these findings, we computed the POD of the streamwise fluctuation vorticity. Analysis of the variance downstream evolution in the different configurations shows that the main effect of the jet, besides increasing the absolute vortex-response variance levels, is in the excitation of a progressively larger number of POD modes. To the best of our knowledge, this finding of a broadband excitation of a multitude of vortex response modes by the jet as a function of spacing is original.

We resume that the jets only have a minor effect on the leading-order statistics of the vortex, i.e., the mean flow and the mean drift path of the vortex centre, while they do significantly affect the unsteady vortex dynamics and this influence is a function of the mutual jet–vortex spacing.

Appendix A: Matching of vortex profile with models

The radial profile of azimuthal and axial mean velocities are fitted to a selection of vortex models that are often used for this purpose [44]. Figure 22 shows the comparison of the vortex profile in the no-jet configuration with the Moore–Saffman and Batchelor models, respectively. The Moore–Saffman model offers the best match for the azimuthal mean velocity, while the axial mean velocity is well represented by both models. The *n* factor of the Moore–Saffman model, representing the decay rate of the azimuthal velocity in the potential flow region, equals approximately 0.8, rather than 1 as expected for the Batchelor vortex and explains the better fitting of the Moore–Saffman model. The same results are found for the jet–vortex configuration $d_{\text{jet}}/b = 0.80$ (not shown).

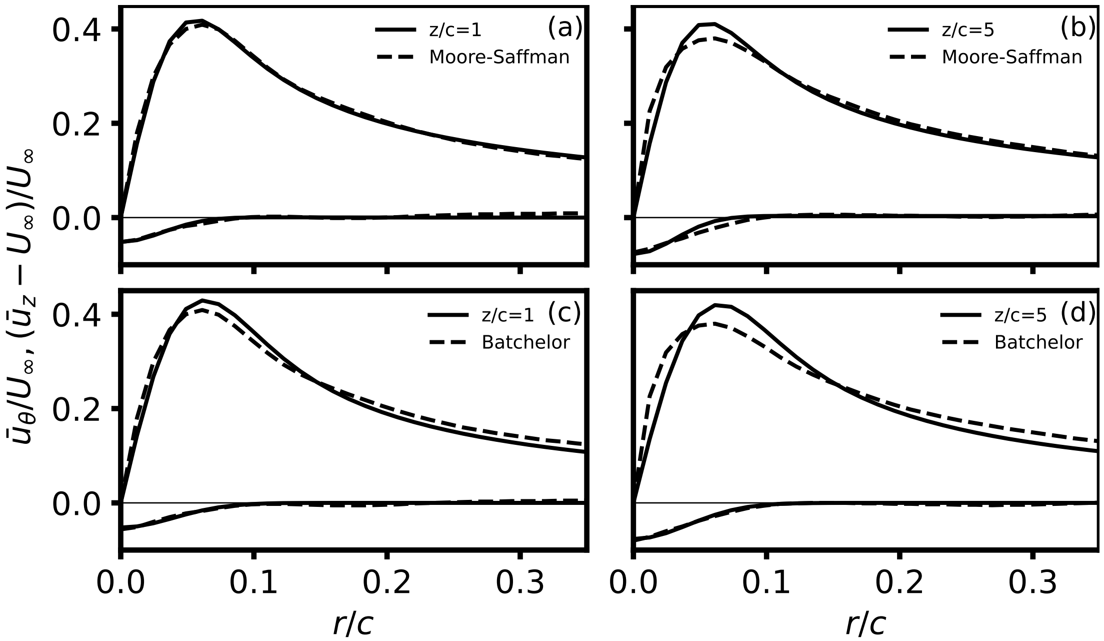

FIG. 22. Comparison of the vortex profile against the Moore– Saffman model for (a) $z/c = 1$ and (b) $z/c = 5$ and the Batchelor vortex for (c) $z/c = 1$ and (d) $z/c = 5$, in the no-jet configuration.

Appendix B: Discussion on the disturbing effect of the jet support structures

As detailed in § II and shown in Fig. 1–2, the jets are installed on bottom-mounted support structures, which *a priori* must be expected to contribute an additional disturbance to the vortex.

In order to estimate the effect of the supports on the vortex, we have conducted additional PIV measurements of the three different configurations $d_{\text{jet}}/b \in \{0.44, 0.58, 0.80\}$ with the jets installed but not blowing. On comparing these results against the same configurations but with the jet switched on and the no-jet case, the disturbing effect of the supports can be estimated.

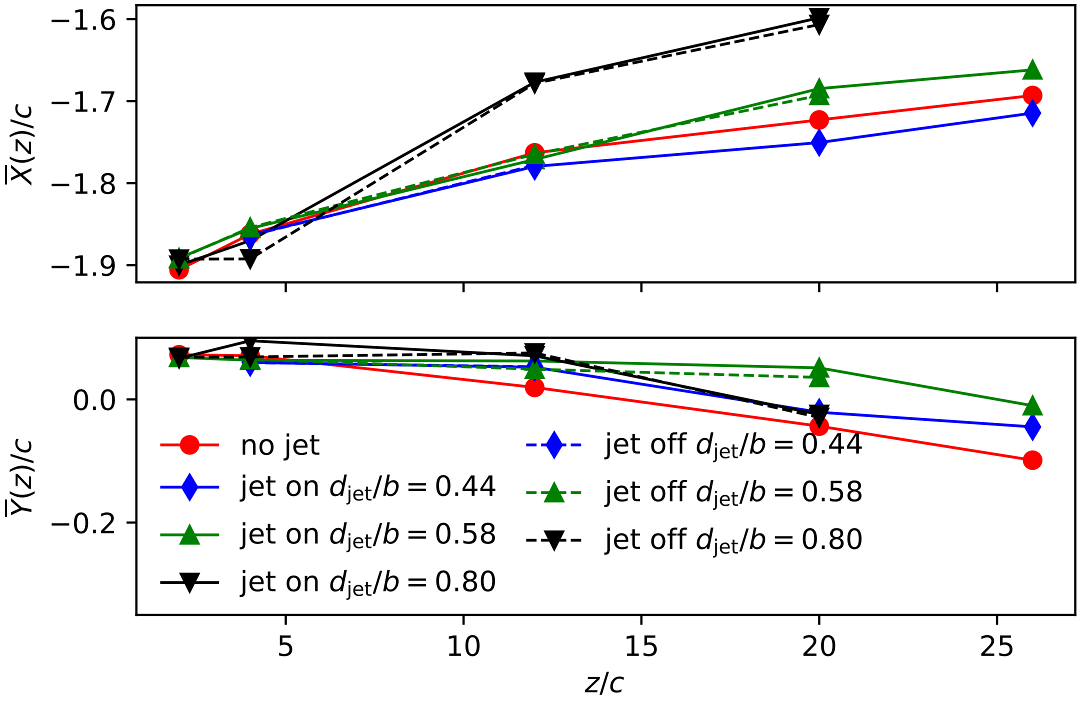

FIG. 23. Downstream evolution of the mean location of the vortex centre for the different configurations, comparing jet-on jet-off.

The distinctly different impact exerted by the supports on the vortex is well illustrated by comparing the leading-order vortex-centre stochastic moments (discussed in § IV) for the seven different configurations, which we call for convenience no-jet, $d_{\text{jet}}/b \in \{0.44, 0.58, 0.80\}$ jet-on and jet-off configurations. Figure 23, displaying the mean drift trajectories of the vortex centre, shows that the variations in the vortex-centre mean location is mainly induced by the supports rather than the jet flow.

However, we find that the fluctuation dynamics, being the main interest of this study, is only insignificantly influenced by the support structures. This is shown in Fig. 24, comparing the standard deviation of the vortex-centre location $\sigma(z) = \sqrt{\sigma_X^2(z) + \sigma_Y^2(z)}$ for the various configurations. Particularly for the $d_{\text{jet}}/b \in \{0.44, 0.58\}$ jet–vortex configurations, the supports have no effect on the vortex fluctuations at all, as the respective curves in Fig. 24 collapse.

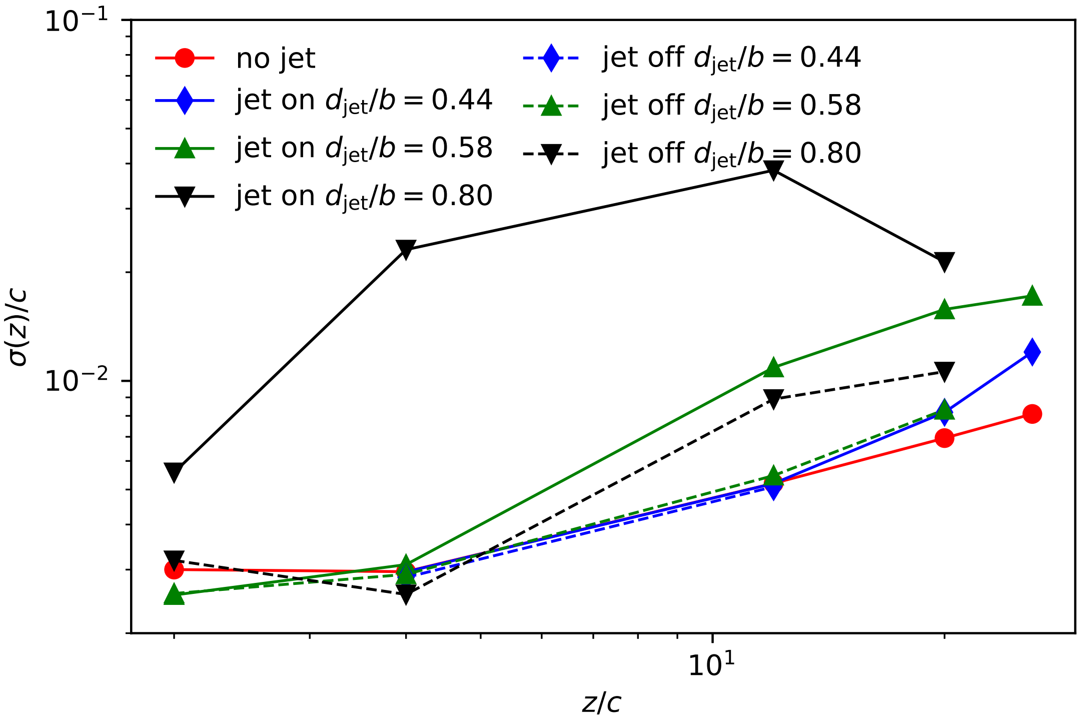

FIG. 24. Downstream evolution of the standard deviation $\sigma(z) = \sqrt{\sigma_X^2(z) + \sigma_Y^2(z)}$ of the vortex centre for the different configurations, comparing jet-on jet-off.

FUNDING SOURCES

This work is based on an experiment which was carried out within the PHYWAKE research project under the funding of the French Ministry for Civil Aviation (DGAC) contract *CONVENTION 2015/03*.

DATA AVAILABILITY

The data that support the findings of this study are available from the corresponding author upon reasonable request.

REFERENCES

[1] T. Gerz, T. Dürbeck, and P. Konopka, “Transport and effective diffusion of aircraft emissions,” Journal of Geophysical Research: Atmospheres **103**, 25905–25913 (1998).

[2] R. Paoli and K. Shariff, "Contrail modeling and simulation," Annual Review of Fluid Mechanics **48** (2016).

[3] T. Gerz, F. Holzäpfel, and D. Darracq, "Commercial aircraft wake vortices," Progress in Aerospace Sciences **38**, 181–208 (2002).

[4] I. Gursul and Z. Wang, "Flow control of tip/edge vortices," AIAA Journal **56**, 1731–1749 (2018).

[5] R. Paoli, J. Helie, and T. Poinsot, "Contrail formation in aircraft wakes," Journal of Fluid Mechanics **502**, 361–373 (2004).

[6] O. Zeman, "The persistence of trailing vortices: a modeling study," Physics of Fluids **7**, 135–143 (1995).

[7] P. R. Spalart, "Airplane trailing vortices," Annual Review of Fluid Mechanics **30**, 107 (1998).

[8] P. Margaris, D. Marles, and I. Gursul, "Experiments on jet/vortex interaction," Experiments in Fluids **44**, 261–278 (2008).

[9] P. Margaris and I. Gursul, "Wing tip vortex control using synthetic jets," The Aeronautical Journal **110**, 673–681 (2006).

[10] F. Blanco-Rodríguez, L. Parras, and C. del Pino, "Frequency response of lamb-oseen vortex," Fluid Dynamics Research **48**, 061417 (2016).

[11] J. H. G. Ortiz, *Experimental study in near-and far-field of trailing vortices and their active control*, Ph.D. thesis, Universidad de Málaga (2017).

[12] M. Dghim, M. Ferchichi, and H. Fellouah, "On the effect of active flow control on the meandering of a wing-tip vortex," Journal of Fluid Mechanics **896** (2020).

[13] M. Zaccara, G. Paolillo, C. S. Greco, T. Astarita, and G. Cardone, "Flow control of wingtip vortices through synthetic jets," Experimental Thermal and Fluid Science **130**, 110489 (2022).

[14] T. Gerz and T. Ehret, "Wake dynamics and exhaust distribution behind cruising aircraft," in *Rep. AGARD CP-584* (NATO, Brussels, 1996).

[15] S. Brunet, F. Garnier, and L. Jacquin, "Numerical/experimental simulation of exhaust jet mixing in wake vortex," in *30th Fluid Dynamics Conference* (1999) p. 3418.

[16] R. Paoli, F. Laporte, B. Cuenot, and T. Poinsot, "Dynamics and mixing in jet/vortex interactions," Physics of fluids **15**, 1843–1860 (2003).

[17] A. Naiman, S. Lele, and M. Jacobson, "Large eddy simulations of contrail development: Sensitivity to initial and ambient conditions over first twenty minutes," Journal of Geophysical Research: Atmospheres **116** (2011).

[18]R. Paoli, L. Nybelen, J. Picot, and D. Cariolle, "Effects of jet/vortex interaction on contrail formation in supersaturated conditions," Physics of Fluids **25**, 053305 (2013).

[19]G. Huppertz, E. Fares, R. Abstiens, and W. Schröder, "Investigation of engine jet/wing-tip vortex interference," Aerospace science and technology **8**, 175–183 (2004).

[20]L. Jacquin, P. Molton, P. Loiret, and E. Coustols, "An experiment on jet-wake vortex interaction," in *37th AIAA Fluid Dynamics Conference and Exhibit* (2007) p. 4363.

[21]F. Champagnat, A. Plyer, G. Le Besnerais, B. Leclaire, S. Davoust, and Y. Le Sant, "Fast and accurate piv computation using highly parallel iterative correlation maximization," Experiments in fluids **50**, 1169–1182 (2011).

[22]S. B. Pope and S. B. Pope, *Turbulent flows* (Cambridge university press, 2000).

[23]H. Tennekes and J. L. Lumley, *A first course in turbulence* (MIT press, 1972).

[24]G. Baker, S. Barker, K. Bofah, and P. Saffman, "Laser anemometer measurements of trailing vortices in water," Journal of Fluid Mechanics **65**, 325–336 (1974).

[25]W. J. Devenport, M. C. Rife, S. I. Liapis, and G. J. Follin, "The structure and development of a wing-tip vortex," Journal of fluid mechanics **312**, 67–106 (1996).

[26]S. Bailey and S. Tavoularis, "Measurements of the velocity field of a wing-tip vortex, wandering in grid turbulence," Journal of Fluid Mechanics **601**, 281–315 (2008).

[27]G. V. Iungo, "Wandering of a wing-tip vortex: rapid scanning and correction of fixed-point measurements," Journal of Aircraft **54**, 1779–1790 (2017).

[28]A. Heyes, R. Jones, and D. Smith, "Wandering of wing-tip vortices," in *Proceedings of 12th international symposium on the applications of laser techniques to fluid mechanics. Lisbon, Portugal* (2004).

[29]J. Elsas and L. Moriconi, "Vortex identification from local properties of the vorticity field," Physics of Fluids **29**, 015101 (2017).

[30]C. Truesdell, "Vorticity averages," Canadian Journal of Mathematics **3**, 69–86 (1951).

[31]P. G. Saffman, *Vortex dynamics* (Cambridge University Press, 1995).

[32]T. Leweke, S. Le Dizes, and C. H. Williamson, "Dynamics and instabilities of vortex pairs," Annual Review of Fluid Mechanics **48**, 507–541 (2016).

[33]A. Sommerfeld, *Vorlesungen über theoretische Physik 2: Mechanik der deformierbaren Medien* (Akademische Verlagsgesellschaft Becker & Erler, 1945).

[34]J. Van Jaarsveld, A. Holten, A. Elsenaar, R. Trieling, and G. Van Heijst, "An experimental study of the effect of external turbulence on the decay of a single vortex and a vortex pair," Journal of

fluid mechanics **670**, 214–239 (2011).

[35]L. Jacquin, D. Fabre, P. Geffroy, and E. Coustols, "The properties of a transport aircraft wake in the extended near field-an experimental study," in *39th Aerospace Sciences Meeting and Exhibit* (2001) p. 1038.

[36]M. Beninati and J. Marshall, "An experimental study of the effect of free-stream turbulence on a trailing vortex," Experiments in Fluids **38**, 244–257 (2005).

[37]A. M. Edstrand, T. B. Davis, P. J. Schmid, K. Taira, and L. N. Cattafesta, "On the mechanism of trailing vortex wandering," Journal of Fluid Mechanics **801** (2016).

[38]H. C. Ghimire and S. C. Bailey, "An experimental investigation of wing-tip vortex decay in turbulence," Physics of Fluids **29**, 037108 (2017).

[39]L. Jacquin and F. Garnier, "On the dynamics of engine jets behind a transport aircraft," in *Rep. AGARD CP-584* (NATO, Brussels, 1996).

[40]C. Heaton, "Centre modes in inviscid swirling flows and their application to the stability of the batchelor vortex," Journal of Fluid Mechanics **576**, 325–348 (2007).

[41]D. Fabre and L. Jacquin, "Viscous instabilities in trailing vortices at large swirl numbers," Journal of Fluid Mechanics **500**, 239–262 (2004).

[42]J. Feys and S. A. Maslowe, "Linear stability of the moore-saffman model for a trailing wingtip vortex," Physics of Fluids **26**, 024108 (2014).

[43]S. Green and A. Acosta, "Unsteady flow in trailing vortices," Journal of Fluid Mechanics **227**, 107–134 (1991).

[44]C. Del Pino, J. Lopez-Alonso, L. Parras, and R. Fernandez-Feria, "Dynamics of the wing-tip vortex in the near field of a naca 0012 aerofoil," The Aeronautical Journal **115**, 229–239 (2011).

[45]S. C. Bailey, S. Pentelow, H. C. Ghimire, B. Estejab, M. A. Green, and S. Tavoularis, "Experimental investigation of the scaling of vortex wandering in turbulent surroundings," Journal of Fluid Mechanics **843**, 722–747 (2018).

[46]W. Phillips and J. Graham, "Reynolds-stress measurements in a turbulent trailing vortex," Journal of Fluid Mechanics **147**, 353–371 (1984).

[47]P. Holmes, J. L. Lumley, and G. Berkooz, *Turbulence, Coherent Structures, Dynamical Systems and Symmetry* (Cambridge University Press, 1996).

[48]L. Sirovich, "Turbulence and the dynamics of coherent structures. i. coherent structures," Quarterly of applied mathematics **45**, 561–571 (1987).

[49]C. Roy and T. Leweke, "Far-wake. fundamental research on aircraft wake phenomena: Experiments on vortex meandering," Tech. Rep. (CNRS-IRPHE, 2008).

[50]M. Karami, H. Hangan, L. Carassale, and H. Peerhossaini, "Coherent structures in tornado-like vortices," Physics of Fluids **31**, 085118 (2019).

[51]F. J. Blanco-Rodríguez, J. O. Rodríguez-García, L. Parras, and C. del Pino, "Optimal response of batchelor vortex," Physics of Fluids **29**, 064108 (2017).

[52]T. Bölle, V. Brion, J.-C. Robinet, D. Sipp, and L. Jacquin, "On the linear receptivity of trailing vortices," Journal of Fluid Mechanics **908** (2021).

[53]P. Gutierrez Castillo, M. Garrido-Martin, T. Bölle, J. H. García-Ortiz, J. Aguilar-Cabello, and C. del Pino, "Higher order dynamic mode decomposition of an experimental trailing vortex," Physics of Fluids (2022).

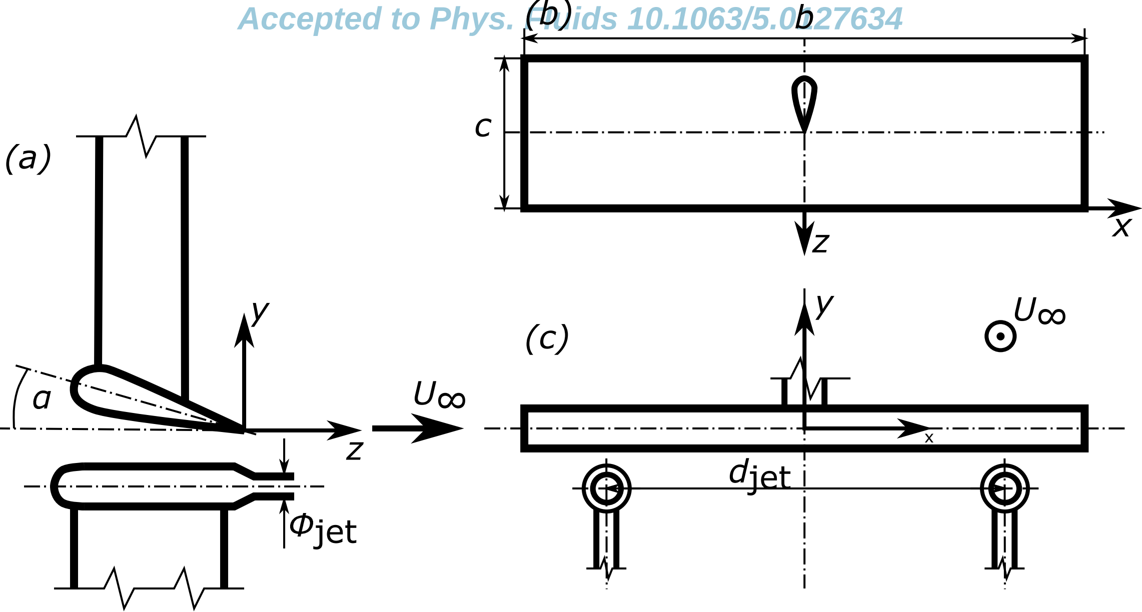
(a)
y
α
z
U∞
Φjet
(b)
b
c
x
z
(c)
y
U∞
x
djet

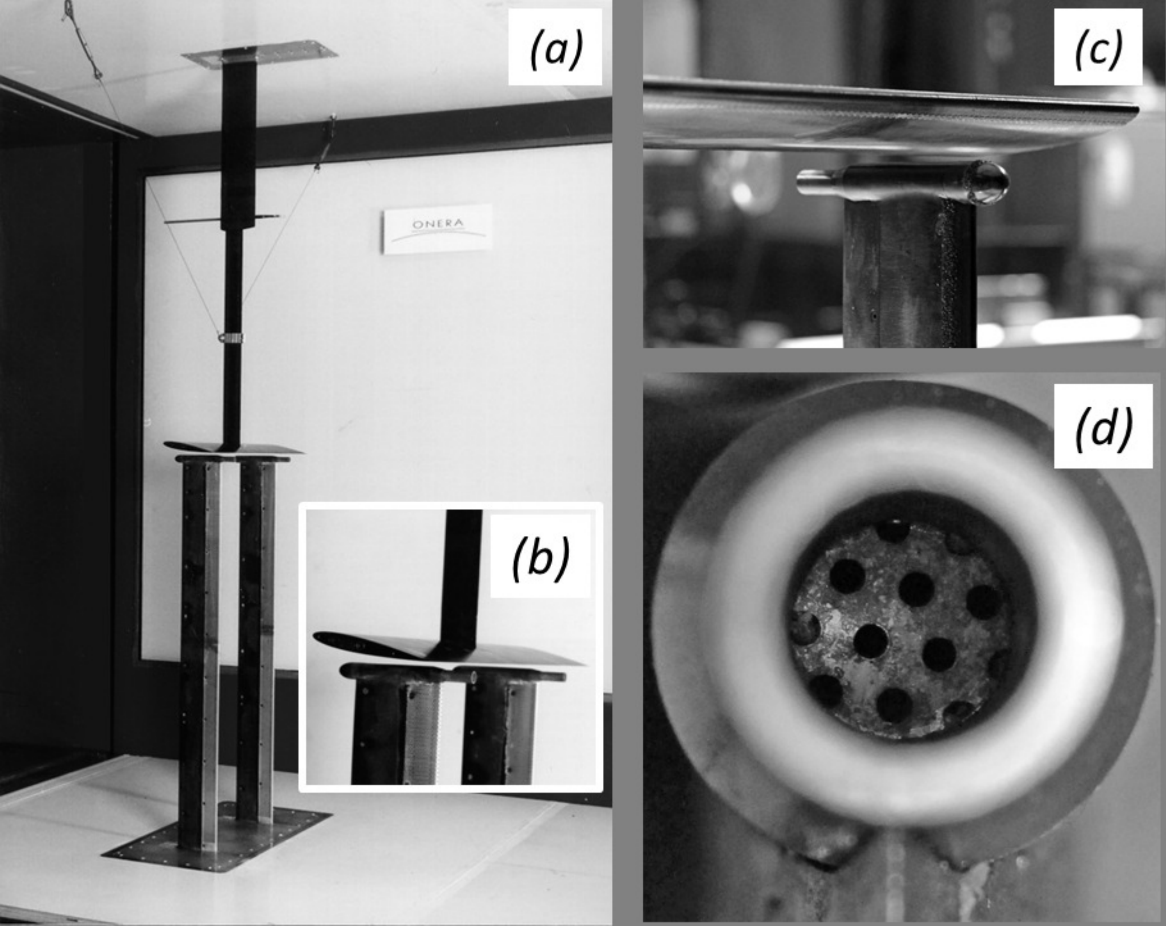
(a)
ONERA
(b)
(c)
(d)

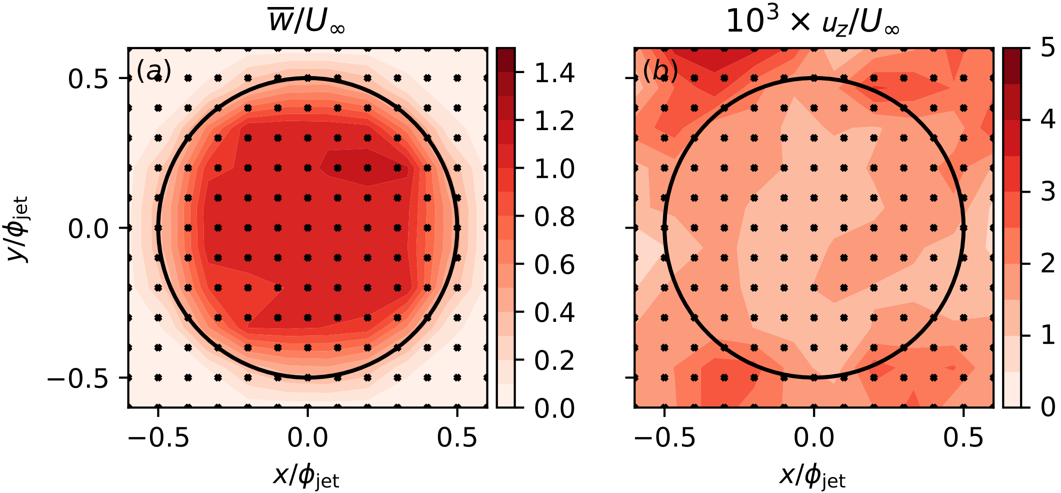
$\overline{w}/U_\infty$
$10^3 \times u_z/U_\infty$
(a)
(b)
0.5
0.0
−0.5
y/ϕ_{jet}
−0.5
0.0
0.5
x/ϕ_{jet}
−0.5
0.0
0.5
x/ϕ_{jet}
1.4
1.2
1.0
0.8
0.6
0.4
0.2
0.0
5
4
3
2
1
0

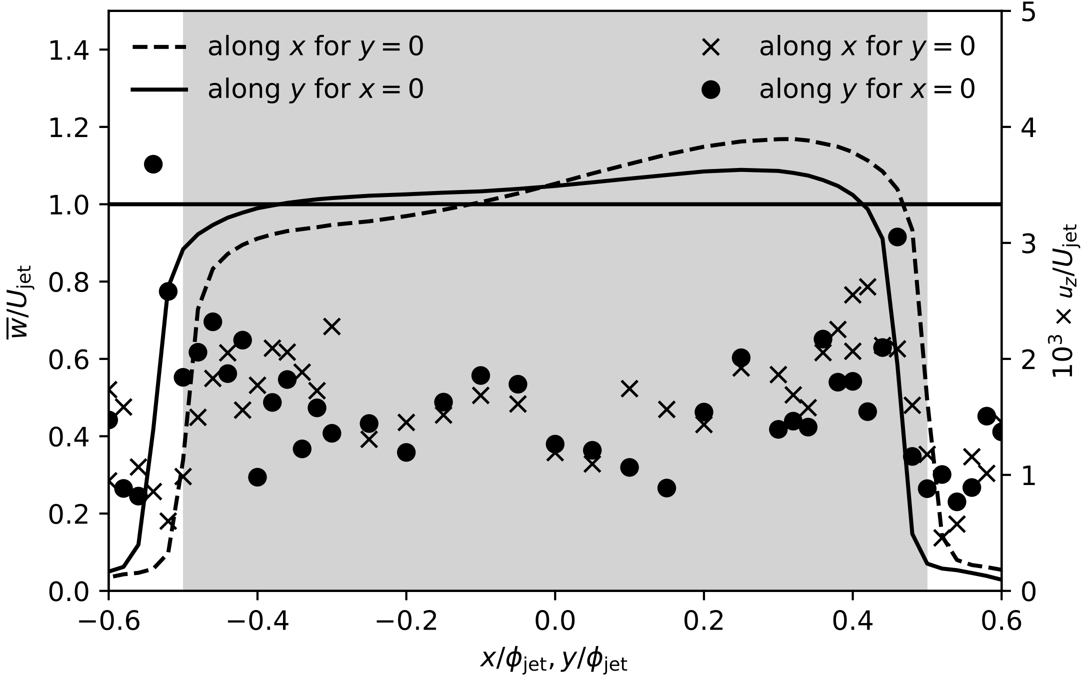
along x for $y = 0$
along y for $x = 0$
along x for $y = 0$
along y for $x = 0$
$\overline{w}/U_{\mathrm{jet}}$
$10^3 \times u_z/U_{\mathrm{jet}}$
$x/\phi_{\mathrm{jet}}, y/\phi_{\mathrm{jet}}$
0.0
0.2
0.4
0.6
0.8
1.0
1.2
1.4
0
1
2
3
4
5
−0.6
−0.4
−0.2
0.0
0.2
0.4
0.6

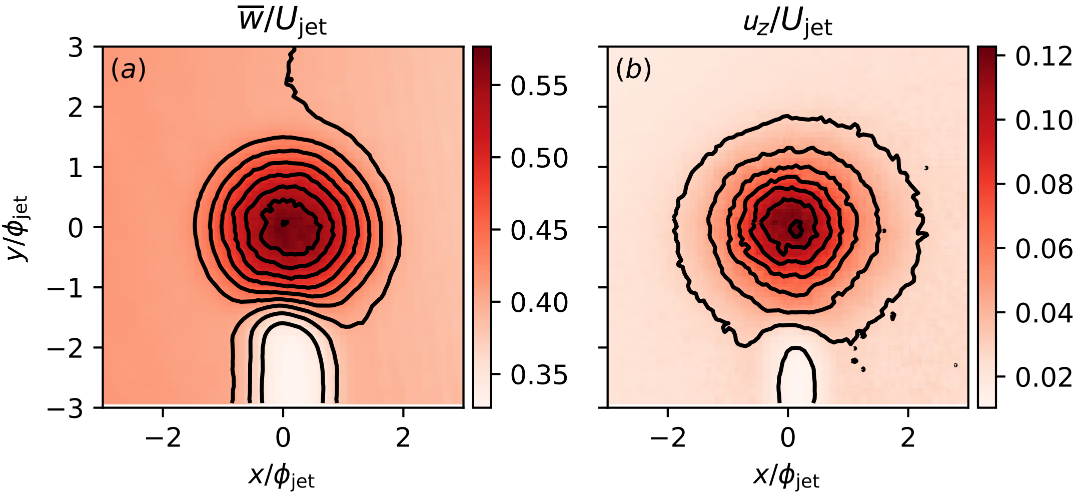
$\overline{w}/U_{\mathrm{jet}}$
u_z/U_{jet}
(a)
(b)
y/ϕ_{jet}
x/ϕ_{jet}
x/ϕ_{jet}
3
2
1
0
−1
−2
−3
−2
0
2
−2
0
2
0.55
0.50
0.45
0.40
0.35
0.12
0.10
0.08
0.06
0.04
0.02

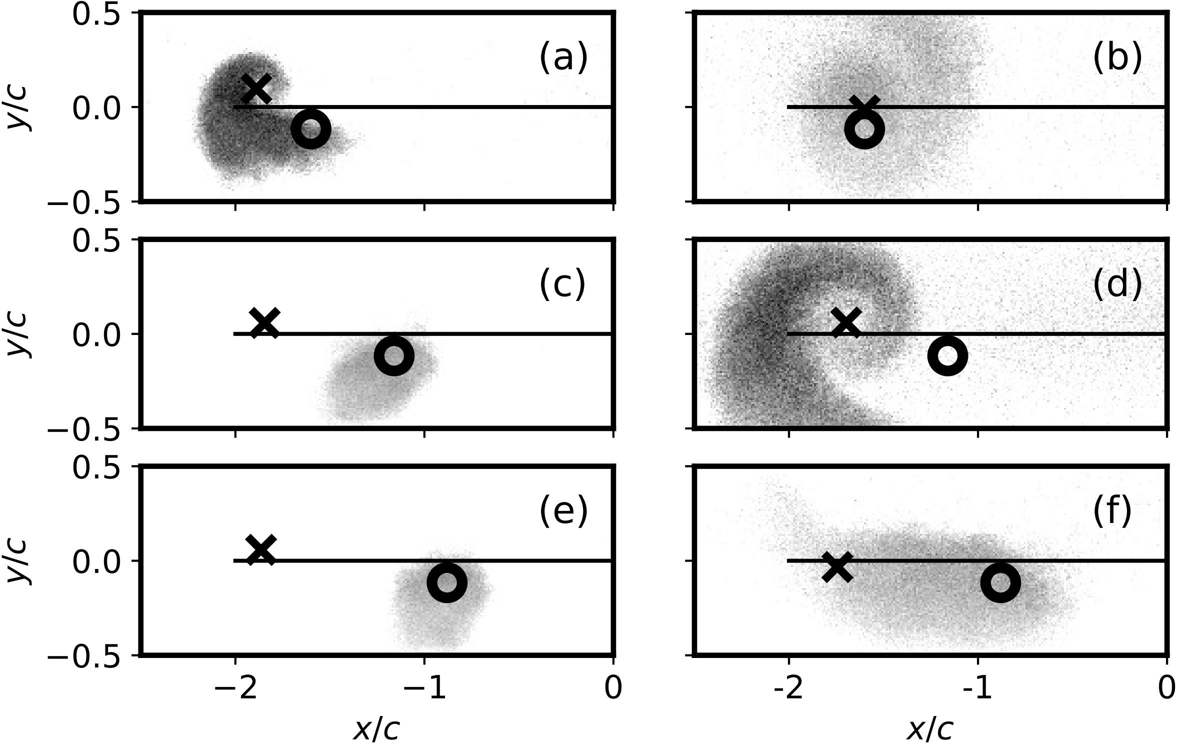
0.5
0.0
−0.5
y/c
(a)
(b)
(c)
(d)
(e)
(f)
−2
−1
0
-2
-1
0
x/c
x/c

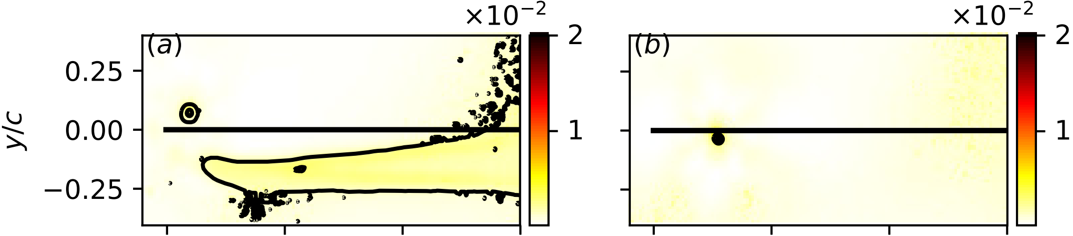
(a)
(b)
y/c
0.25
0.00
−0.25
$\times 10^{-2}$
2
1
$\times 10^{-2}$
2
1

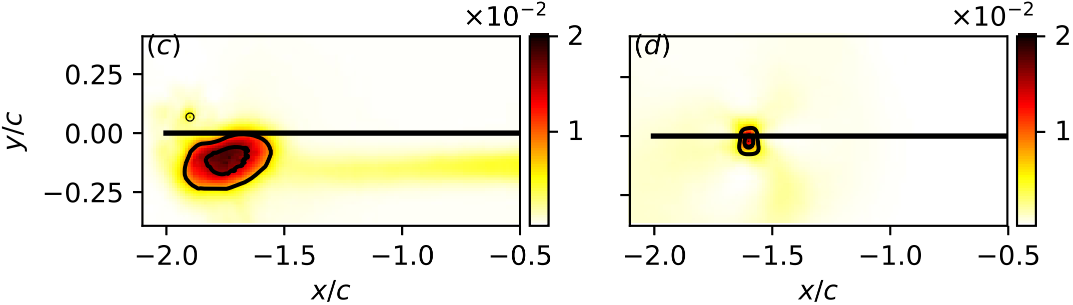
(c)
(d)
×10⁻²
2
1
×10⁻²
2
1
0.25
0.00
−0.25
y/c
−2.0
−1.5
−1.0
−0.5
x/c
−2.0
−1.5
−1.0
−0.5
x/c

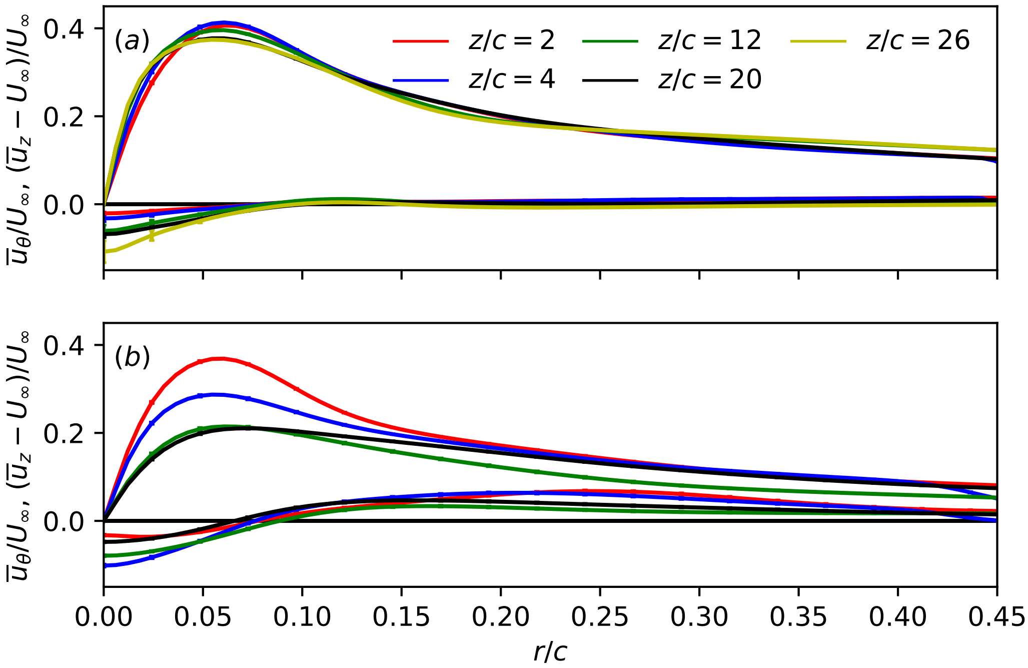
(a)
(b)
$z/c = 2$
$z/c = 4$
$z/c = 12$
$z/c = 20$
$z/c = 26$
$\overline{u}_\theta/U_\infty$, $(\overline{u}_z - U_\infty)/U_\infty$
0.4
0.2
0.0
0.00
0.05
0.10
0.15
0.20
0.25
0.30
0.35
0.40
0.45
r/c

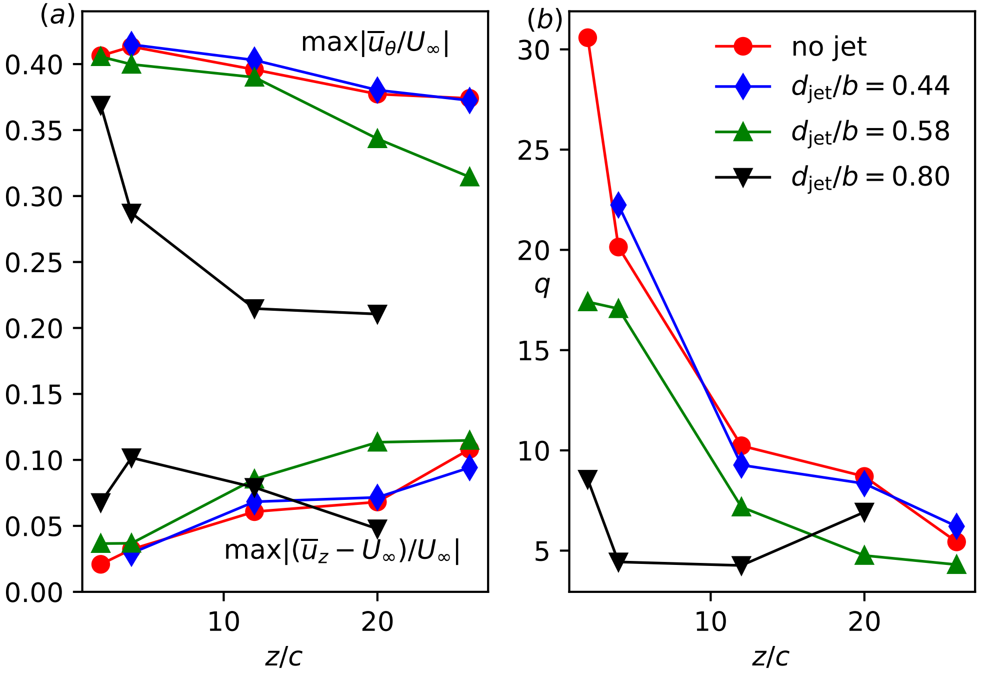
(a)
max$|\overline{u}_\theta/U_\infty|$
max$|(\overline{u}_z-U_\infty)/U_\infty|$
0.00
0.05
0.10
0.15
0.20
0.25
0.30
0.35
0.40
10
20
z/c
(b)
q
5
10
15
20
25
30
10
20
z/c
no jet
$d_{\rm jet}/b=0.44$
$d_{\rm jet}/b=0.58$
$d_{\rm jet}/b=0.80$

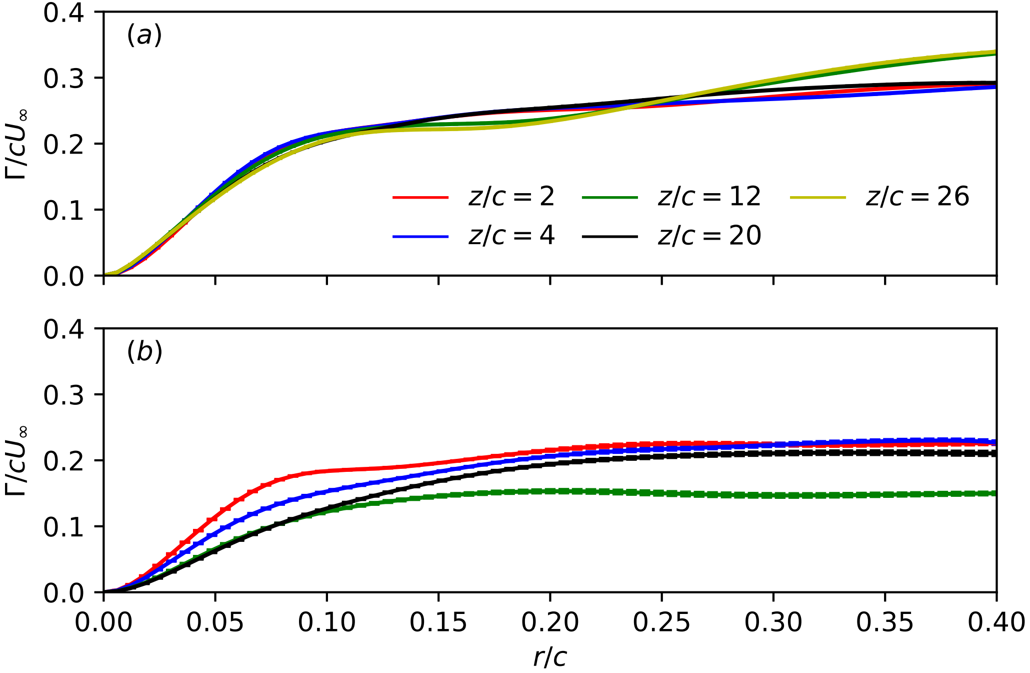
(a)
(b)
Γ/cU_∞
Γ/cU_∞
r/c
0.0
0.1
0.2
0.3
0.4
0.00
0.05
0.10
0.15
0.20
0.25
0.30
0.35
0.40
$z/c = 2$
$z/c = 4$
$z/c = 12$
$z/c = 20$
$z/c = 26$

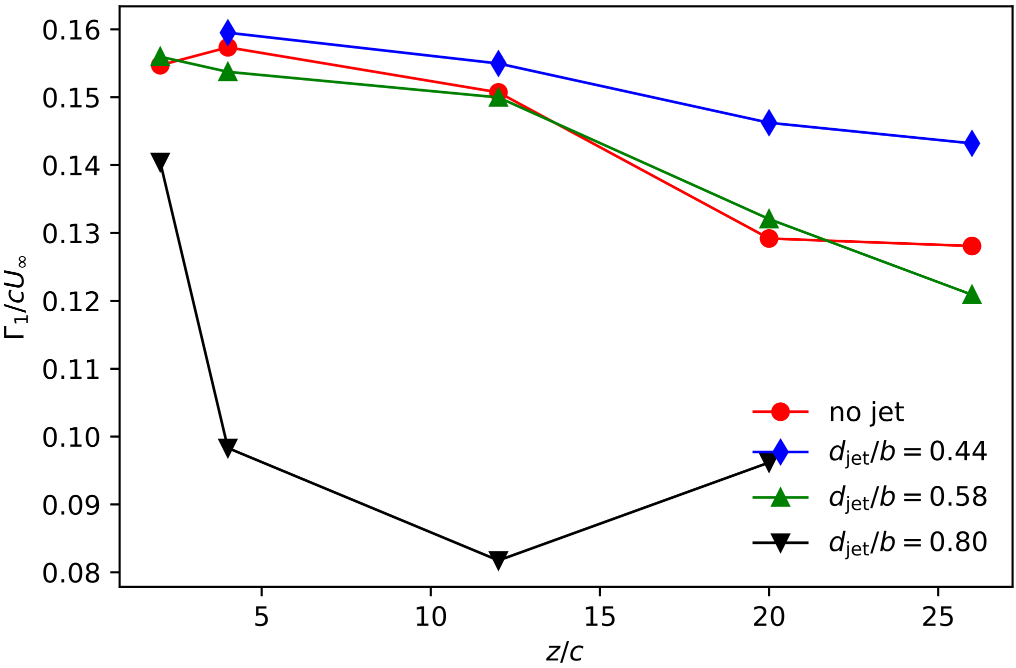
Γ_1/cU_∞
0.16
0.15
0.14
0.13
0.12
0.11
0.10
0.09
0.08
5
10
15
20
25
z/c
no jet
$d_{\mathrm{jet}}/b = 0.44$
$d_{\mathrm{jet}}/b = 0.58$
$d_{\mathrm{jet}}/b = 0.80$

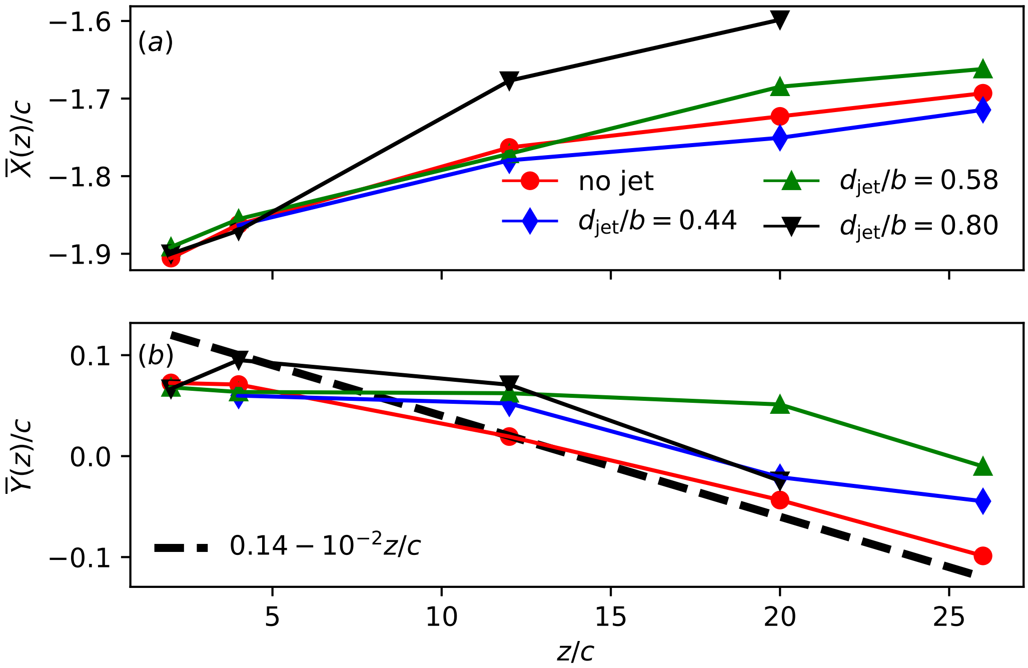
(a)
−1.6
−1.7
−1.8
−1.9
$\overline{X}(z)/c$
no jet
$d_{\rm jet}/b = 0.44$
$d_{\rm jet}/b = 0.58$
$d_{\rm jet}/b = 0.80$
(b)
0.1
0.0
−0.1
$\overline{Y}(z)/c$
$0.14 - 10^{-2} z/c$
5
10
15
20
25
z/c

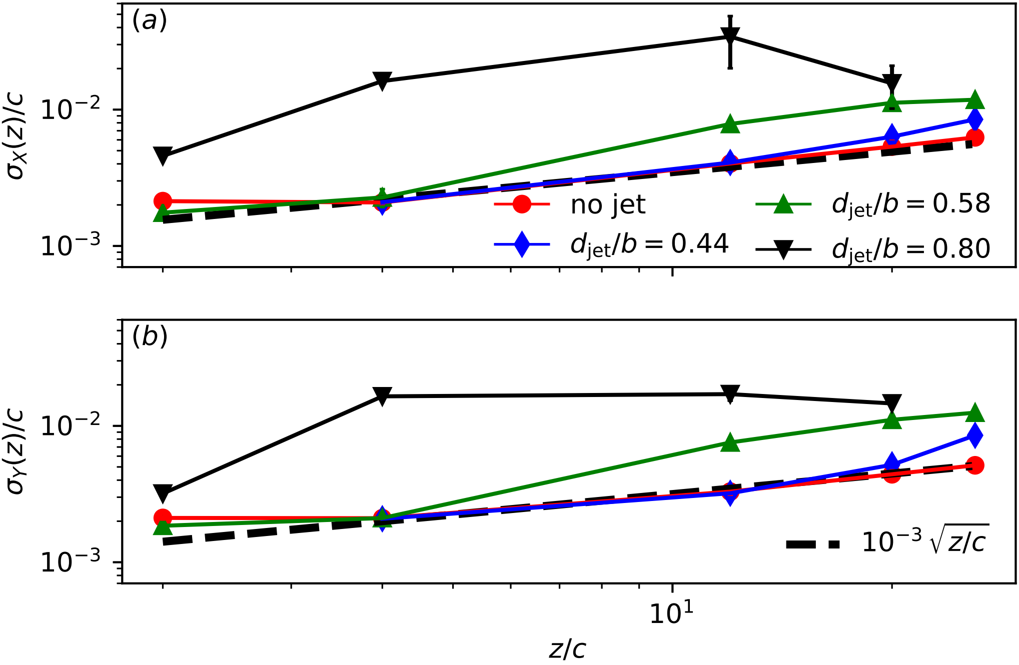
(a)
$\sigma_X(z)/c$
10^{-2}
10^{-3}
no jet
$d_{\rm jet}/b = 0.44$
$d_{\rm jet}/b = 0.58$
$d_{\rm jet}/b = 0.80$
(b)
$\sigma_Y(z)/c$
10^{-2}
10^{-3}
$10^{-3}\sqrt{z/c}$
10^1
z/c

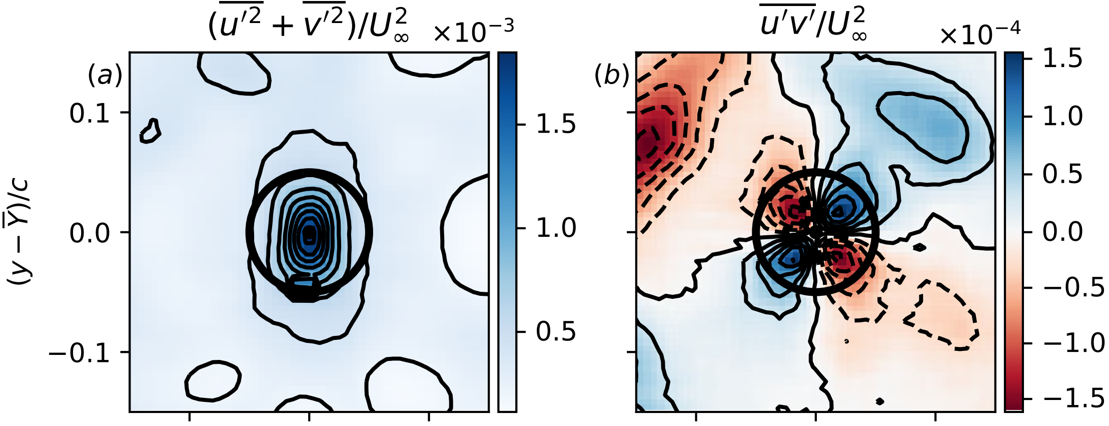
$(\overline{u'^2}+\overline{v'^2})/U_\infty^2$
$\times10^{-3}$
(a)
0.1
0.0
−0.1
$(y-\overline{Y})/c$
1.5
1.0
0.5
$\overline{u'v'}/U_\infty^2$
$\times10^{-4}$
(b)
1.5
1.0
0.5
0.0
−0.5
−1.0
−1.5

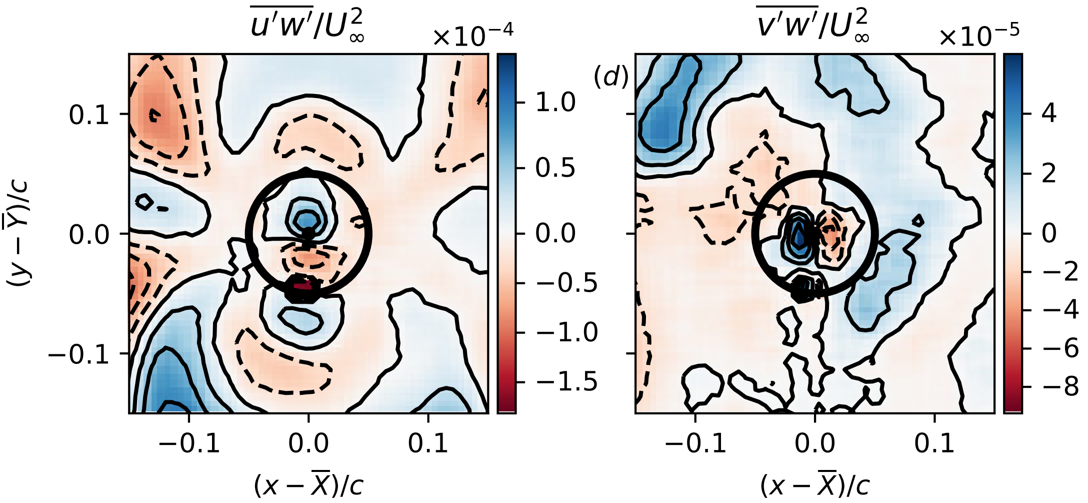

$\overline{u'w'}/U_\infty^2$
$\times10^{-4}$
1.0
0.5
0.0
−0.5
−1.0
−1.5
0.1
0.0
−0.1
$(y-\overline{Y})/c$
−0.1
0.0
0.1
$(x-\overline{X})/c$
$\overline{v'w'}/U_\infty^2$
$\times10^{-5}$
(d)
4
2
0
−2
−4
−6
−8
−0.1
0.0
0.1
$(x-\overline{X})/c$

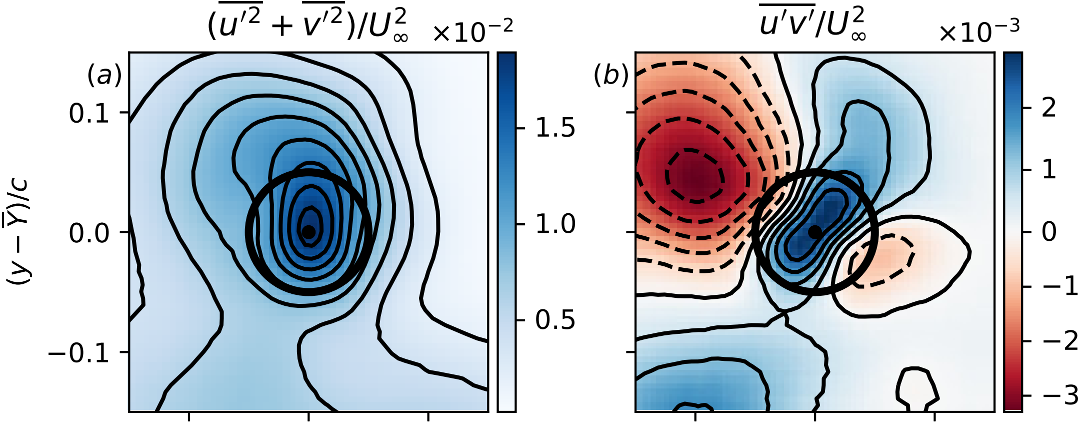
$(\overline{u'^2}+\overline{v'^2})/U_\infty^2$
$\times 10^{-2}$
(a)
0.1
0.0
−0.1
$(y-\overline{Y})/c$
1.5
1.0
0.5
$\overline{u'v'}/U_\infty^2$
$\times 10^{-3}$
(b)
2
1
0
−1
−2
−3

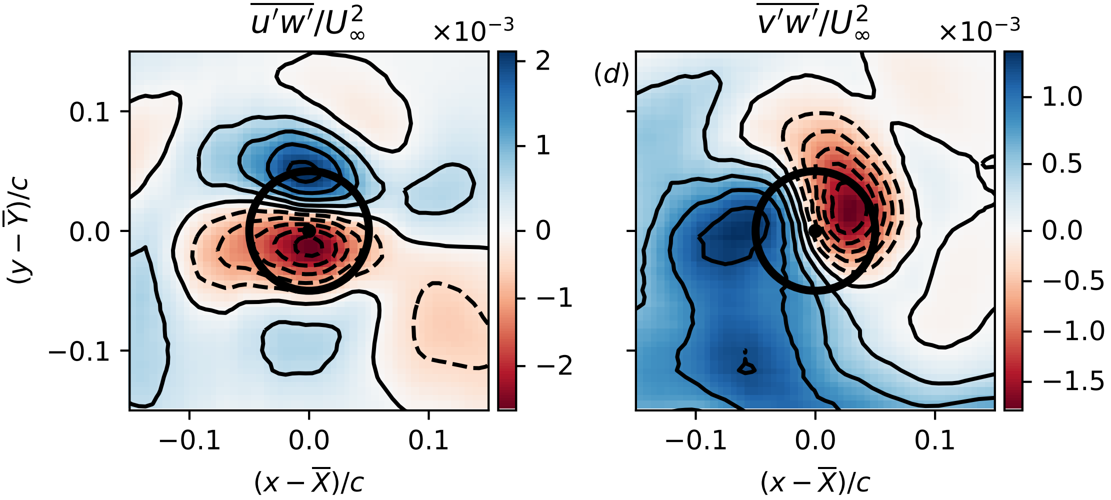
$\overline{u'w'}/U_\infty^2$
$\times10^{-3}$
2
1
0
−1
−2
$(y-\overline{Y})/c$
0.1
0.0
−0.1
−0.1
0.0
0.1
$(x-\overline{X})/c$
$\overline{v'w'}/U_\infty^2$
$\times10^{-3}$
(d)
1.0
0.5
0.0
−0.5
−1.0
−1.5
−0.1
0.0
0.1
$(x-\overline{X})/c$

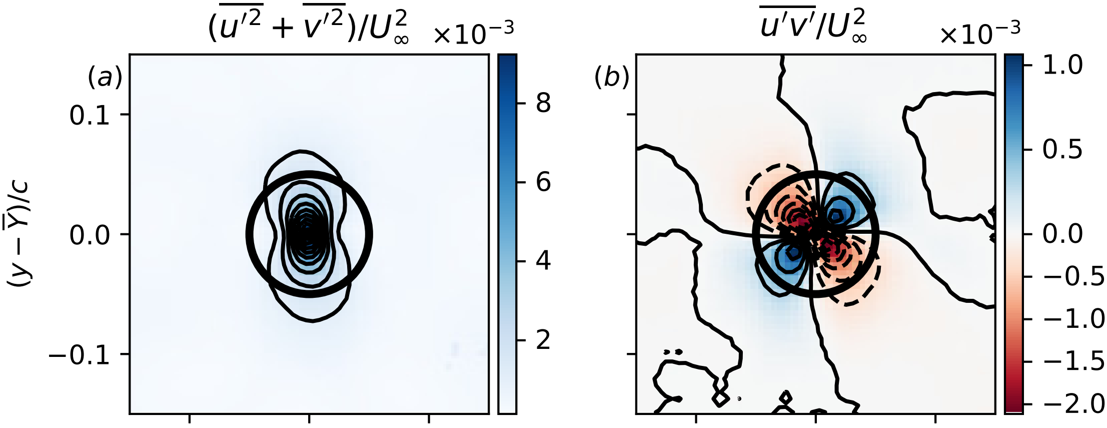
$(\overline{u'^2}+\overline{v'^2})/U_\infty^2$
$\times 10^{-3}$
(a)
0.1
0.0
−0.1
$(y-\overline{Y})/c$
8
6
4
2
$\overline{u'v'}/U_\infty^2$
$\times 10^{-3}$
(b)
1.0
0.5
0.0
−0.5
−1.0
−1.5
−2.0

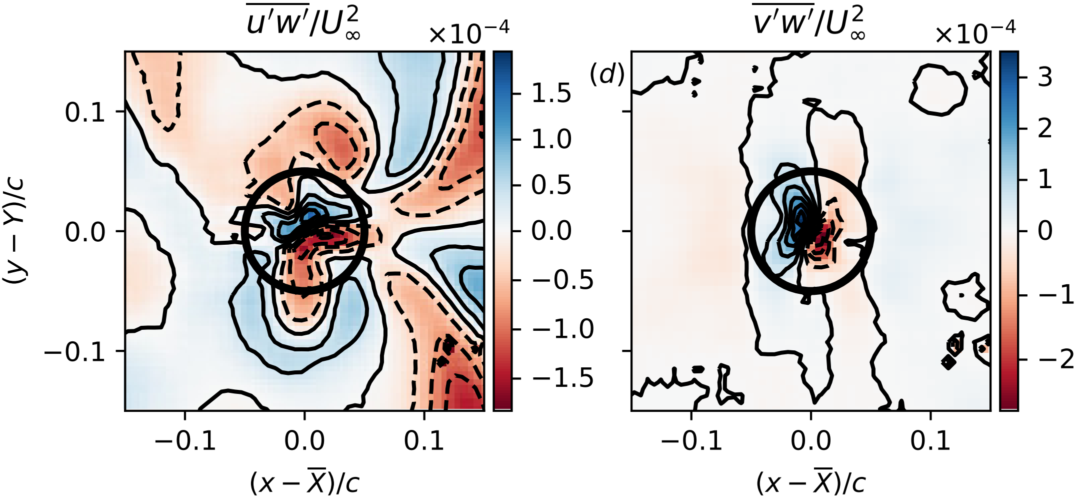
$\overline{u'w'}/U_\infty^2$
$\times10^{-4}$
1.5
1.0
0.5
0.0
−0.5
−1.0
−1.5
0.1
0.0
−0.1
$(y-\overline{Y})/c$
−0.1
0.0
0.1
$(x-\overline{X})/c$
$\overline{v'w'}/U_\infty^2$
$\times10^{-4}$
(d)
3
2
1
0
−1
−2
−0.1
0.0
0.1
$(x-\overline{X})/c$

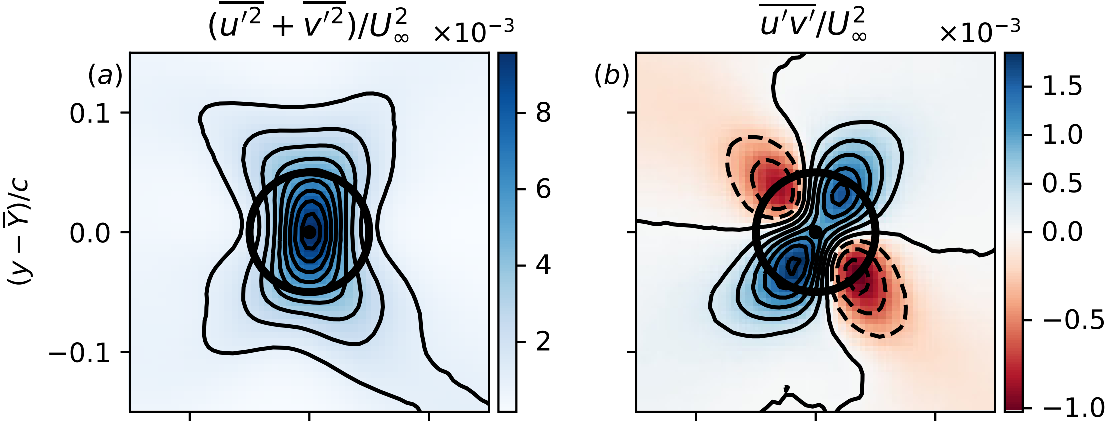
$(\overline{u'^2}+\overline{v'^2})/U_\infty^2$
$\times10^{-3}$
(a)
0.1
0.0
−0.1
$(y-\overline{Y})/c$
8
6
4
2
$\overline{u'v'}/U_\infty^2$
$\times10^{-3}$
(b)
1.5
1.0
0.5
0.0
−0.5
−1.0

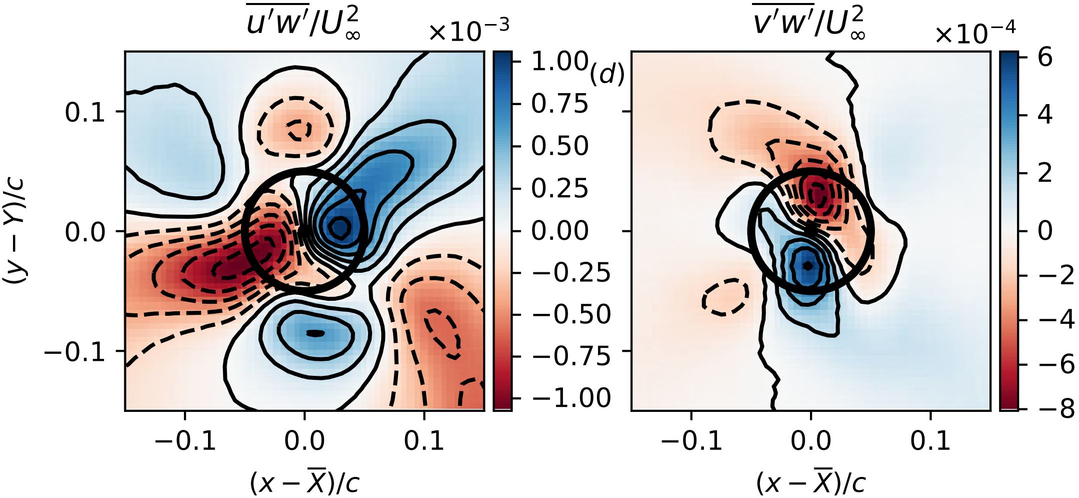
$\overline{u'w'}/U_\infty^2$
$\times 10^{-3}$
1.00
0.75
0.50
0.25
0.00
−0.25
−0.50
−0.75
−1.00
$(y-\overline{Y})/c$
0.1
0.0
−0.1
−0.1
0.0
0.1
$(x-\overline{X})/c$
(d)
$\overline{v'w'}/U_\infty^2$
$\times 10^{-4}$
6
4
2
0
−2
−4
−6
−8
−0.1
0.0
0.1
$(x-\overline{X})/c$

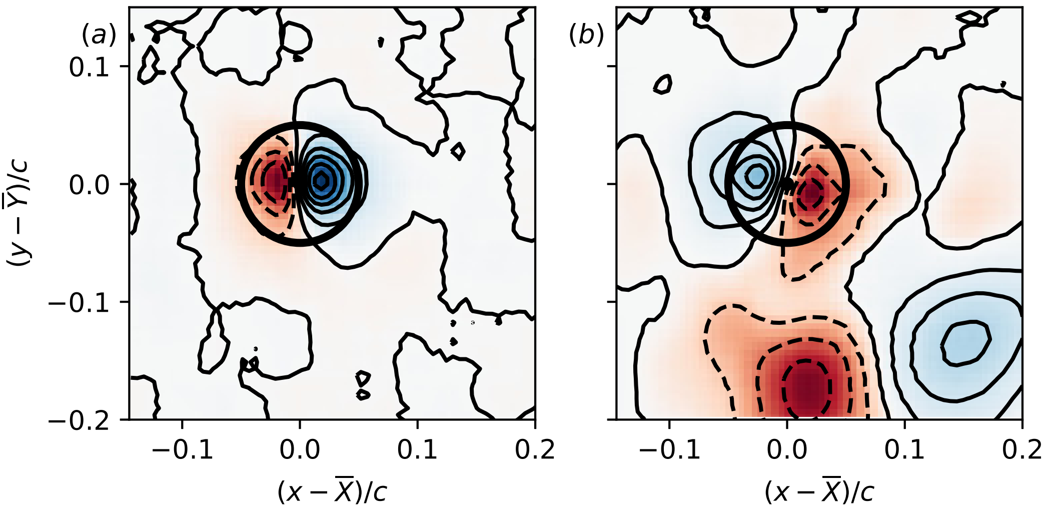
(a)
(b)
0.1
0.0
−0.1
−0.2
$(y-\overline{Y})/c$
−0.1
0.0
0.1
0.2
$(x-\overline{X})/c$
−0.1
0.0
0.1
0.2
$(x-\overline{X})/c$

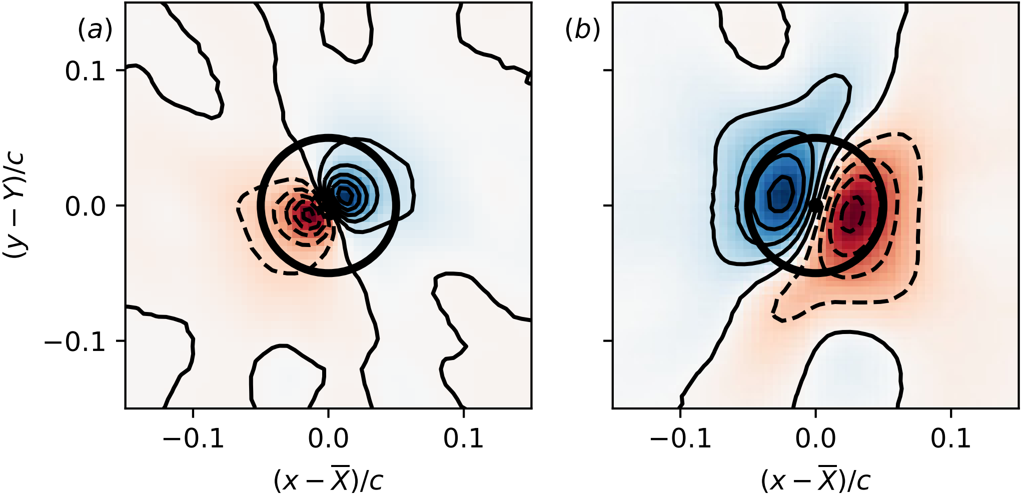
(a)
(b)
0.1
0.0
−0.1
$(y-\overline{Y})/c$
−0.1
0.0
0.1
$(x-\overline{X})/c$
−0.1
0.0
0.1
$(x-\overline{X})/c$

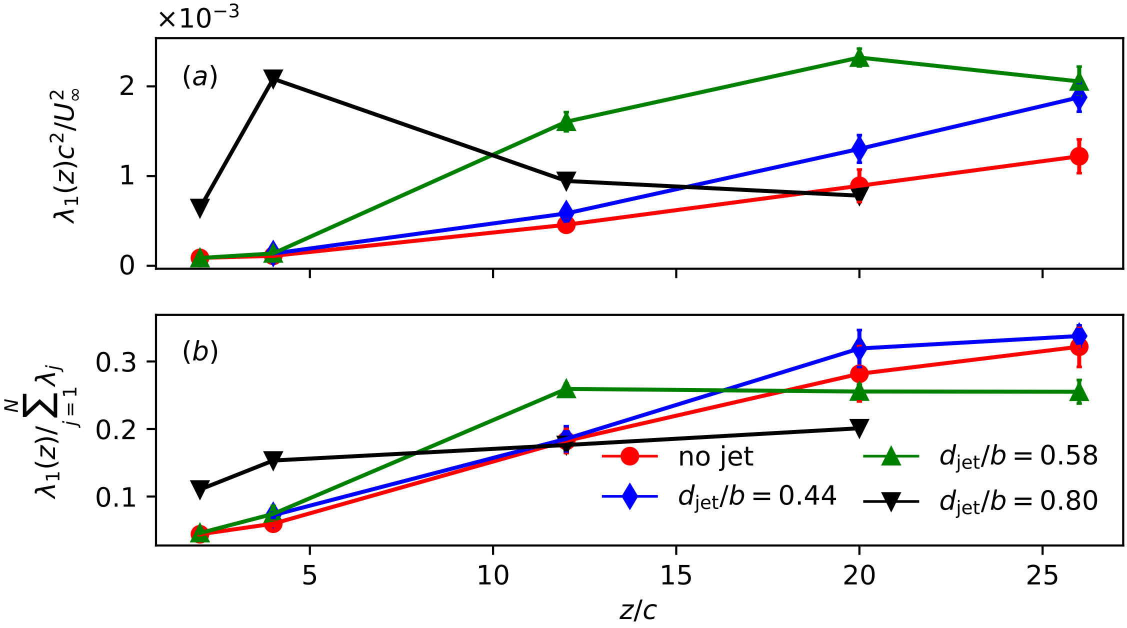
$\times 10^{-3}$
(a)
$\lambda_1(z)c^2/U_\infty^2$
0
1
2
(b)
$\lambda_1(z)/\sum_{j=1}^{N}\lambda_j$
0.1
0.2
0.3
no jet
$d_{\mathrm{jet}}/b = 0.44$
$d_{\mathrm{jet}}/b = 0.58$
$d_{\mathrm{jet}}/b = 0.80$
5
10
15
20
25
z/c

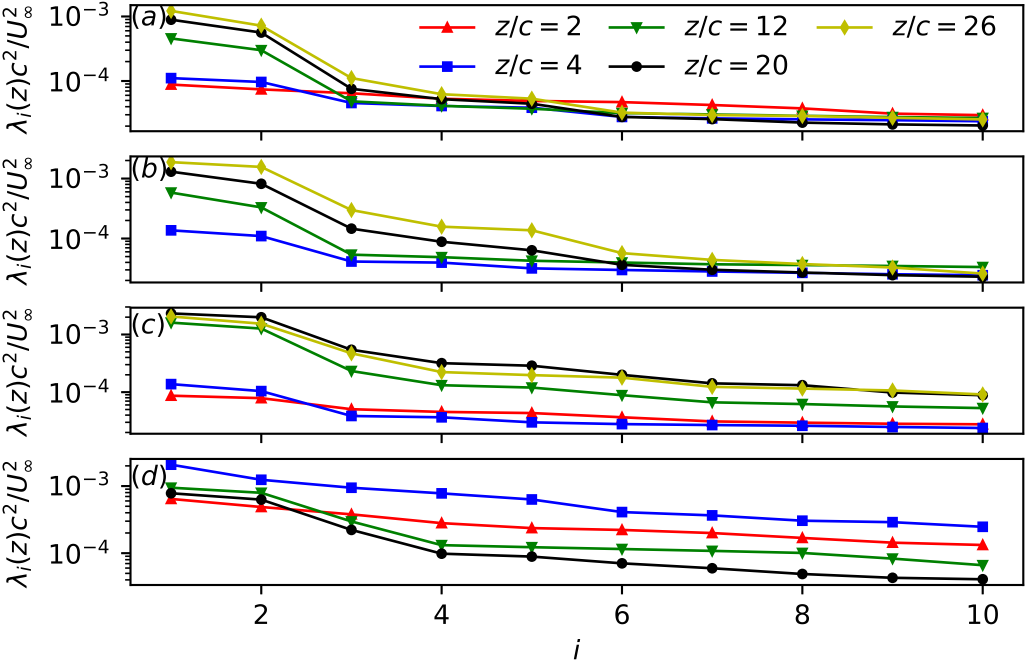
(a)
(b)
(c)
(d)
$\lambda_i(z)c^2/U_\infty^2$
10^{-3}
10^{-4}
$z/c = 2$
$z/c = 4$
$z/c = 12$
$z/c = 20$
$z/c = 26$
2
4
6
8
10
i

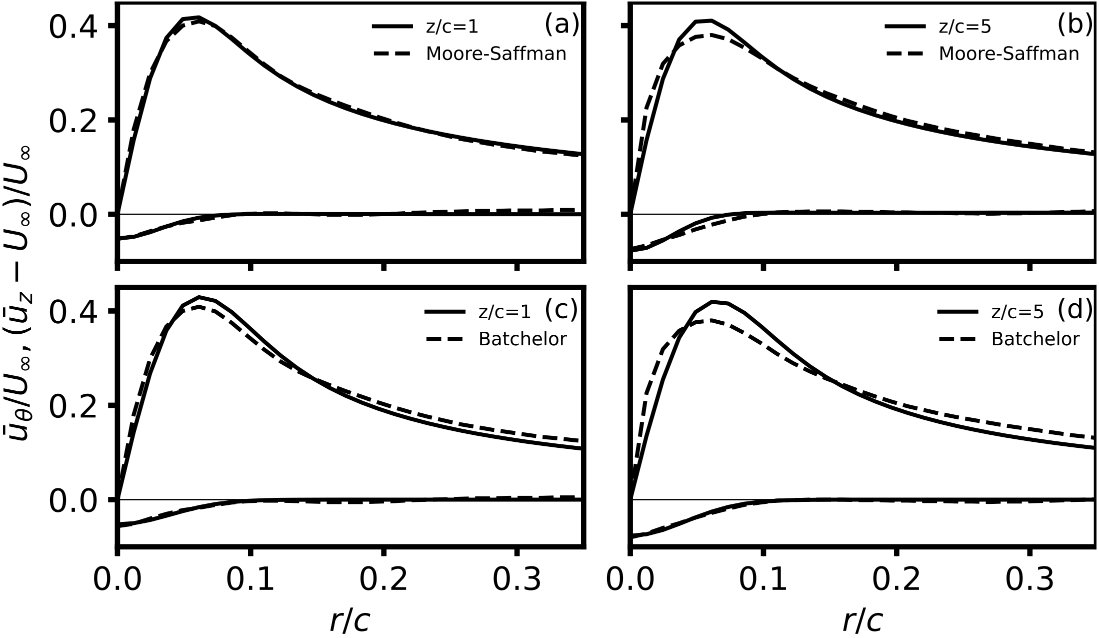

$\bar{u}_\theta/U_\infty$, $(\bar{u}_z - U_\infty)/U_\infty$
0.4
0.2
0.0
0.0
0.1
0.2
0.3
r/c
r/c
(a)
z/c=1
Moore-Saffman
(b)
z/c=5
Moore-Saffman
(c)
z/c=1
Batchelor
(d)
z/c=5
Batchelor

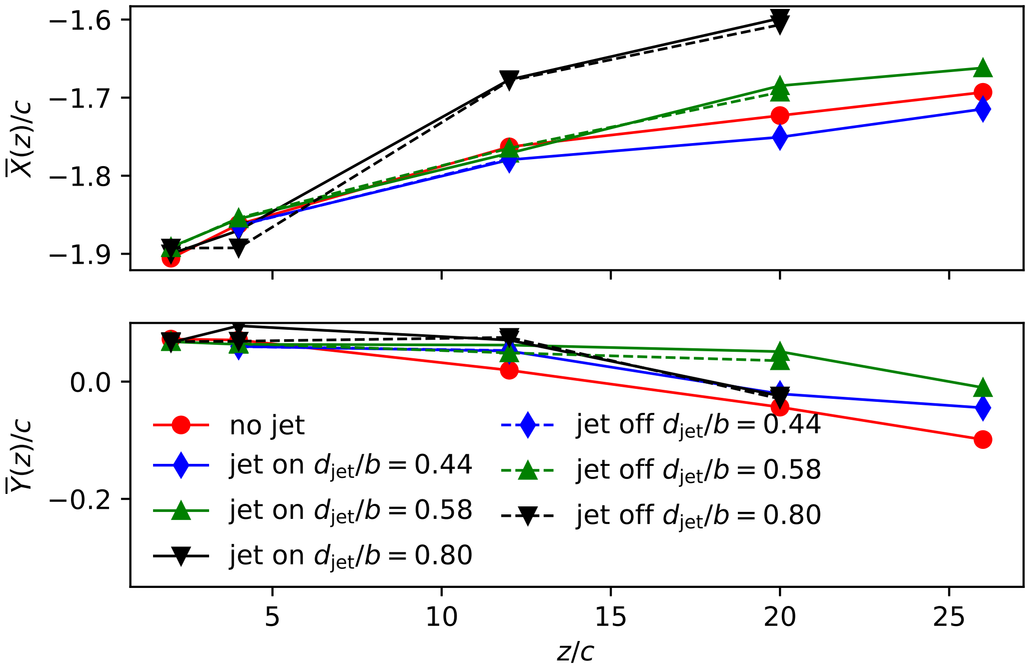
−1.6
−1.7
−1.8
−1.9
$\overline{X}(z)/c$
0.0
−0.2
$\overline{Y}(z)/c$
5
10
15
20
25
z/c
no jet
jet on $d_{\mathrm{jet}}/b = 0.44$
jet on $d_{\mathrm{jet}}/b = 0.58$
jet on $d_{\mathrm{jet}}/b = 0.80$
jet off $d_{\mathrm{jet}}/b = 0.44$
jet off $d_{\mathrm{jet}}/b = 0.58$
jet off $d_{\mathrm{jet}}/b = 0.80$

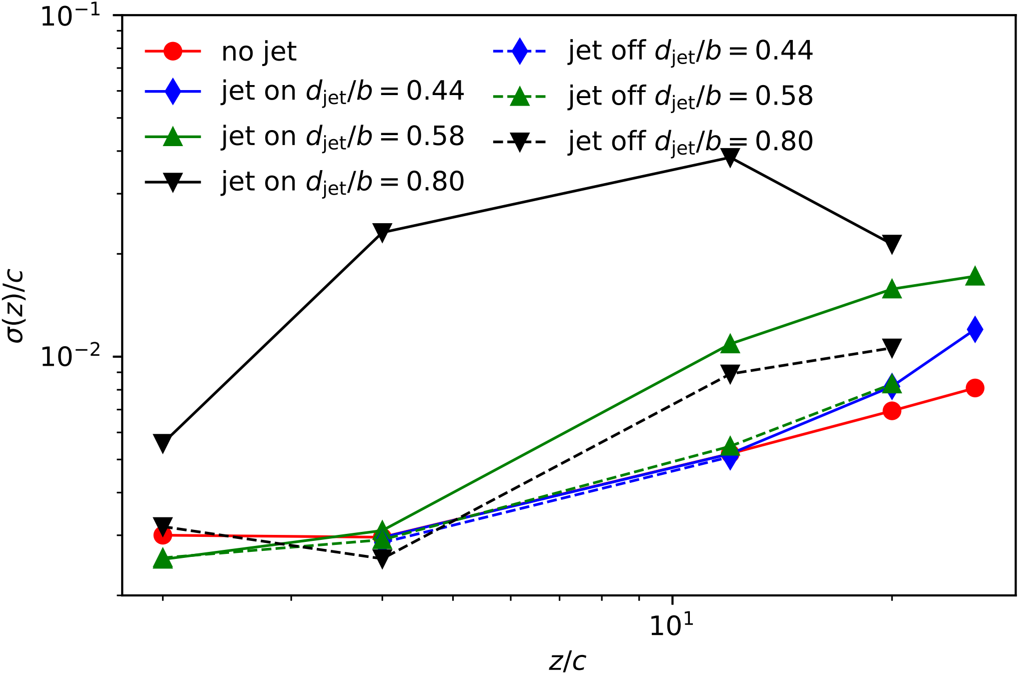
10^{-1}
10^{-2}
10^{1}
$\sigma(z)/c$
z/c
no jet
jet on $d_{\mathrm{jet}}/b = 0.44$
jet on $d_{\mathrm{jet}}/b = 0.58$
jet on $d_{\mathrm{jet}}/b = 0.80$
jet off $d_{\mathrm{jet}}/b = 0.44$
jet off $d_{\mathrm{jet}}/b = 0.58$
jet off $d_{\mathrm{jet}}/b = 0.80$